CHAPTER 4

MORPHOLOGY DEVELOPMENT OF CRYSTALLIZABLE TERPOLYMERS OF L-LACTIDE, ε-CAPROLACTONE AND GLYCOLIDE

4.1 Introduction

Copolymers of L-lactide with units such as ε-caprolactone and glycolide have been proposed and used in a wide variety of biomedical applications, as mentioned in chapter 1. The properties can be tailored to particular applications by adjusting the chemical configuration of the polymers in terms of the monomers used and their composition together with the thermal and mechanical treatments employed during the processing of the products. In many circumstances, the key to tailor the properties is the control of crystallization of the polymer. Homopolymers of L-lactide exhibit a number of crystalline phases whose structures have been determined from X-ray patterns of highly aligned fibres. A particular phase displayed appears to depend on the processing route of fibres. The most common structure is α-phase which exhibits a -10/3 helical chain conformation [82-84]. However, when the fibre is drawn at higher temperature to a higher draw ratio, β-phase which is based on a -3/1 helix is found [85-86]. As with many helical structures, interactions between neighbouring chains play an important part in stabilising particular structures and detailed work by Puiggali et al. has identified specific frustrated packing schemes that arise from differing parallel and antiparallel arrangements of neighbouring chains [82, 86-87]. In the case of terpolymers which contain 70 mol% or more of L-lactide in random and equivalent sequence lengths in block terpolymers may exhibit some crystallinity. Clearly the local chain environment in a random terpolymer may differ greatly from that in a homopolymer system. This contribution therefore focuses on determining the structural characteristics of the crystalline component of such terpolymer fibres drawn under various conditions, as shown in Table 3.3. These are complex materials with a number of components and phases. Analysis of the X-ray diffraction data is not at all straightforward, even from highly aligned fibres. We then have developed a new approach which facilitates the comparison of data from partially oriented, poorly ordered systems. In particular, we compare those for the random and block terpolymers with that for poly(L-lactide) [88] to explore if the -10/3 helical chain conformation in crystalline of poly(L-lactide) is replicated in these terpolymers.

4.2 Instrumental methods for structural characterization

4.2.1 X-ray scattering techniques

X-ray scattering techniques are frequently applied to study microstructures in polymer fibres to investigate phenomena of polymer deformation, orientation and structure formation. In a linear polymer, the monomers are joined together by covalent bonds along the macromolecular chains. These chains may pack together side-by-side and lie along one particular direction in a small crystallite. The size of crystallite is governed by the nature and the conditions at crystallization. Each crystallite, called a lamella, may aligned in any direction as shown in Fig. 1.10. For such a crystalline polymer, an X-ray diffraction pattern occurs from correlations between the regular repeatition of the unit cells that are packed together in parallel planes of lamellae. Fig. 4.1 shows two parallel planes of atoms, AA' and BB', which have the same Miller's indices *h, k, l* and separated by the inter-planar spacing d_{hkl}. The scattering of a coherent monochromatic radiation of wavelength λ at and angle θ will be governed by Bragg's Law as below.

$$d_{hkl} = \frac{\lambda}{2\sin\theta} \tag{4.1}$$

or

$$d_{hkl} = \frac{2\pi}{Q} \tag{4.2}$$

where Q is the scattering vector related to scattering angle 2θ by the relation of $Q = \dfrac{4\pi \sin\theta}{\lambda}$

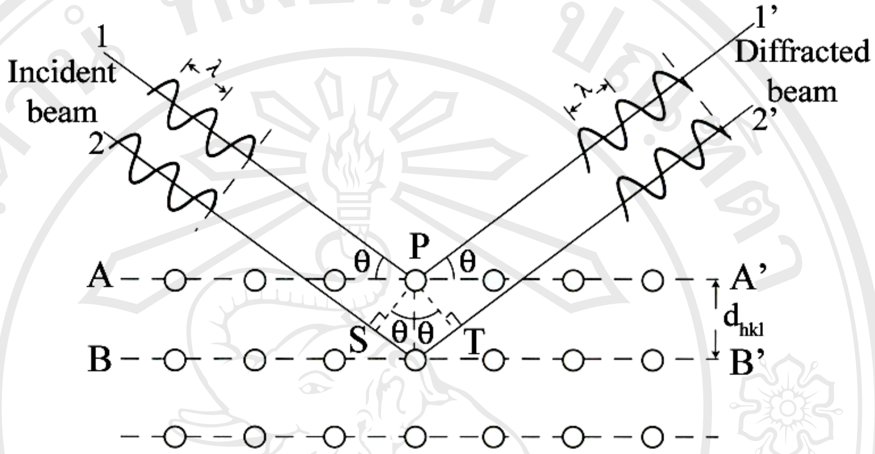

Fig. 4.1 Diffraction of scattering radiation from a series of parallel planes of atoms [89].

The information obtained from the scattered radiation is divided into two types in terms of the polymeric structural features. One is the structural information over the length scales of 1-100Å, which is obtained from the scattering collected from about 10-180° (wide-angle X-ray scattering, WAXS). Second is that in the range of 100-1000Å, obtained from the scattering at less than 1°(small-angle X-ray scattering, SAXS).

4.2.1.1 Wide-angle X-ray scattering (WAXS)

Wide-angle X-ray scattering refers to studies of scattering at relatively large angles. Fig. 4.2 shows a schematic of wide-angle X-ray diffractometer and cameras. The applications of WAXS in polymer are presented in this section. First of all, WAXS provides direct evidence of the physical structure [11]. A typical X-ray diffraction pattern of an unorientated semi-crystalline polymer is shown in Fig. 4.3.

The sample is isotropic, having been crystallized from the melt by lowering the temperature without any application of deformation. It contains many crystallites oriented in all directions with equal probabilities and, as a consequence, exhibits circular diffraction patterns. If the sample is stretched uniaxially after it has been crystallized so that the crystallites in it are highly oriented, the diffraction pattern obtained may look like the one shown in Fig. 4.4. If the degree of orientation of the crystallites is much more modest, the circles of the diffraction such as those in Fig. 4.3 are modified into arcs. The length of such arcs then gives a measure of the degree of crystallite orientation [90].

WAXS is also useful for assessment of crystallinity. The degree of crystallinity may be determined from a WAXS pattern of the randomly oriented semi-crystalline polymer. Fig.4.5 shows an X-ray diffractometer scan of unoriented cotton cellulose, which are recorded between $2\theta = 3$ and 60° after background subtraction. The scattering can be divided into two components due to the crystalline and amorphous structures. On the assumption of that both densities of crystalline and amorphous are approximately equal, the degree of crystallinity (χ) is given by

$$\chi = \frac{I_c}{I_a + I_c} \times 100\% \tag{4.3}$$

where I_c and I_a are the total intensity scattered by the crystalline and amorphous regions respectively [91]. In addition, the broadening of the diffraction peaks provides information about the crystal size.

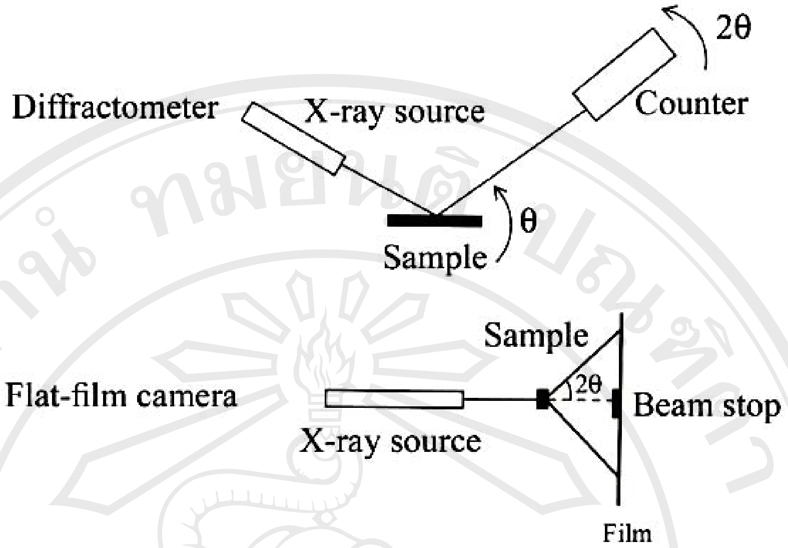

Fig. 4.2 Schematic arrangements in wide-angle X-ray diffractometers and cameras [11].

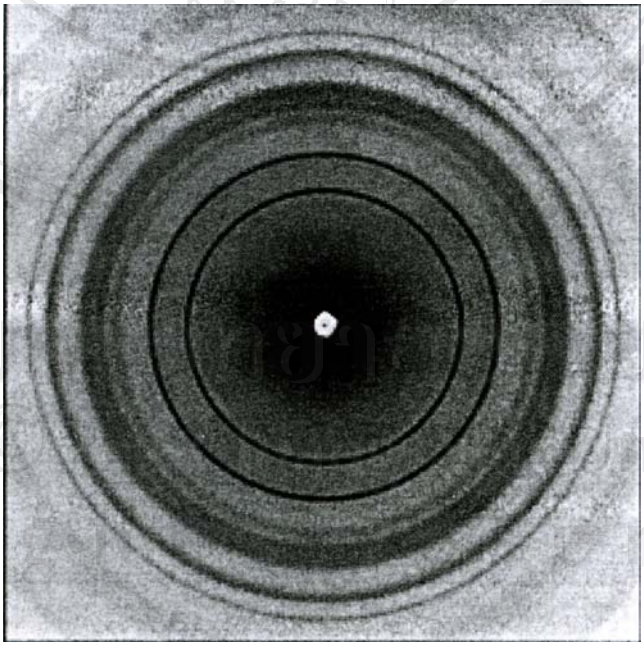

Fig. 4.3 An X-ray diffraction pattern obtained from an isotropic, semi-crystalline polymer of poly(3-hydroxybutyrate) [90].

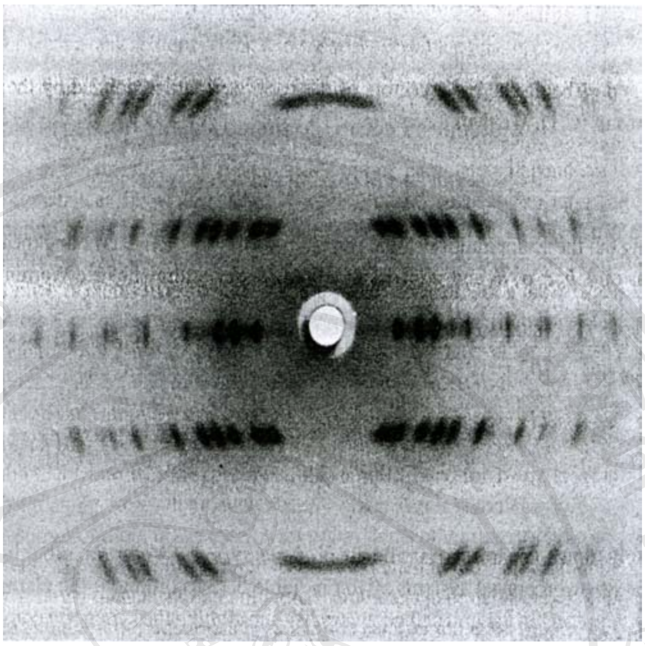

Fig. 4.4 An X-ray diffraction pattern obtained from a highly stretched poly(α,α'-dimethylpropiolactone) fibre [90].

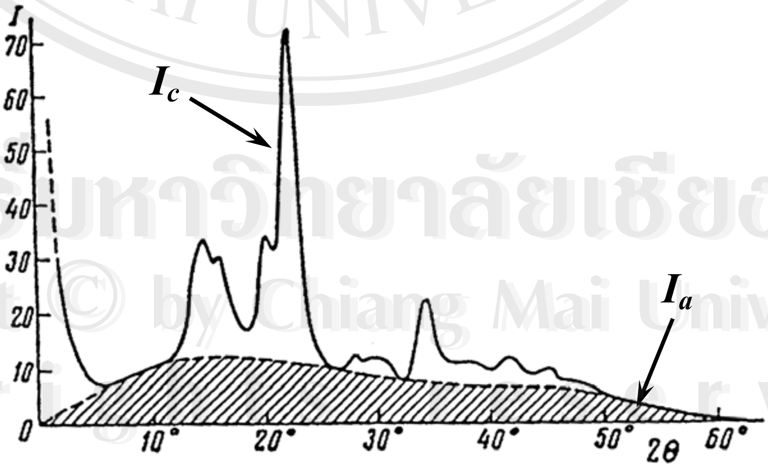

Fig. 4.5 X-ray diffractometer scan of unoriented cotton cellulose showing separation into crystalline and amorphous contribution [92].

In the case of a sample which has been stretched uniaxially (referred to as an extension axis), its morphology is modified as seen in Fig. 3.17. If we consider each crystallite or lamellae as an anisotropic unit, its direction is forced to align along the extension axis as shown in Fig. 4.6. However, in general, the alignment is not perfect. As seen in Fig. 4.6, there is a spread of orientations about the extension axis. It can be described by an angular distribution of the units in polar coordinates ($\boldsymbol{r}$,α), where the alpha, α, being the angle between the structural unit axis and the extension axis, and the length parameter, $\boldsymbol{r}$ is proportional to the number of units at the angle α or probability of angular distribution $D(\alpha)$. Fig. 4.7 shows the shape of surface as a two-dimensional section representing the probability of angular distribution, $D(\alpha)$. This distribution is cylindrical symmetry and is simply described the orientation with a single angle, α. If there was no preferred orientation of the structural units, the surface would be spherical. In addition, the symmetry of a uniaxial system results in the distribution function extending over 0 to 90°, the other three quadrants being equivalent, e.g. Fig. 4.7. For this type of orientation configuration, its orientation distribution function, $D(\alpha)$, varies with α as shown in Fig. 4.8 and its shape represents the level of preferred orientation. The shape of probability distribution function can be analyzed into spherical harmonics, as below.

Fig. 4.6 Anisotropic units with a preferred orientation about an extension axis [96].

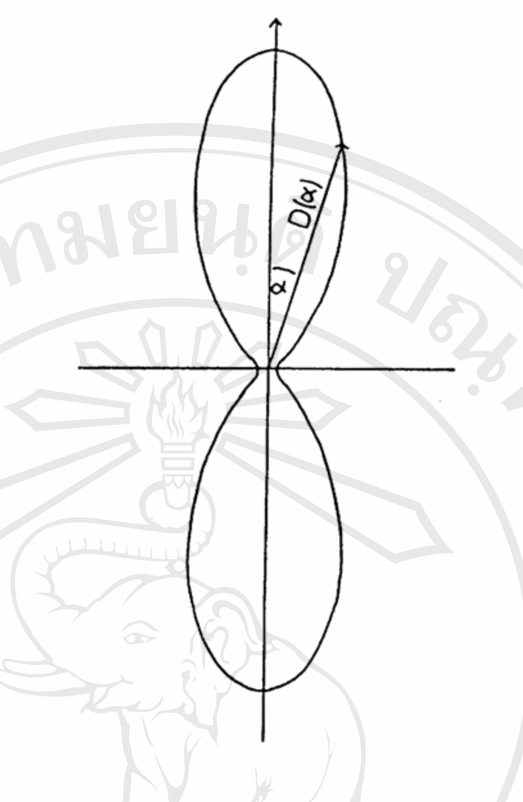

Fig. 4.7 A section through a polar probability plot of a uniaxial orientation distribution [96].

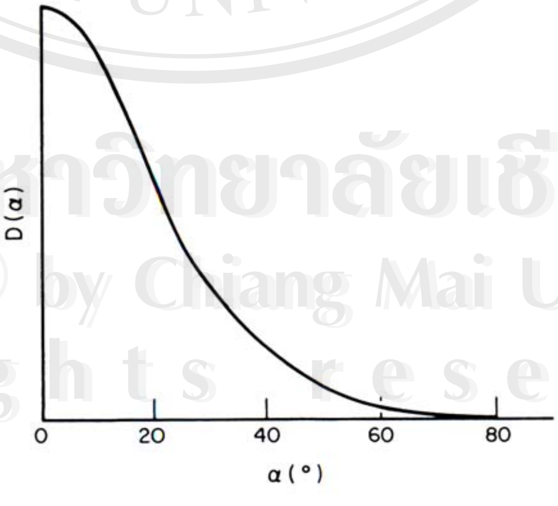

Fig. 4.8 The orientation distribution function, $D(\alpha)$, which represents the level of preferred orientation in Fig.4.6 and 4.7 [95].

$$D(\alpha)=\sum_{n=0}^{\infty}(4n+1)\langle P_{2n}(\cos\alpha)\rangle P_{2n}(\cos\alpha) \tag{4.4}$$

The $(4n+1)$ term is required to maintain the orthogonality of the harmonics where n represents a sequential numbering of the components (n = 0,1,2,3…∞). $P_{2n}(\cos\alpha)$ are in fact the spherical harmonic components and are even members series, odd components not being required for a shape of this surface which shows mirror symmetry about a plane normal to the axis of rotation. The first four components, abbreviated P_0, $P_2(\cos\alpha)$, $P_4(\cos\alpha)$ and $P_6(\cos\alpha)$ or simply P_0, P_2, P_4, P_6, are defined below.

$$\left.\begin{aligned} P_0 &= 1 \\ P_2 &= \left(3\cos^2\alpha-1\right)/2 \\ P_4 &= \left(35\cos^4\alpha-30\cos^2\alpha+3\right)/8 \\ P_6 &= \left(231\cos^6\alpha-315\cos^4\alpha+105\cos^2\alpha-5\right)/16 \end{aligned}\right\} \tag{4.5}$$

The term $\langle P_{2n}(\cos\alpha)\rangle$ is the amplitude of each harmonic, sometimes abbreviated $\langle P_{2n}\rangle$. It is written in brackets to signify an average. The amplitude of a harmonic is determined by integrating the product of the actual function and the harmonic component, in the case over all orientations. The amplitude of the *n*th order harmonic, which is inverted from equation 4.4 is:

$$\langle P_{2n}(\cos\alpha)\rangle = \int_{\textit{all orientation}} D(\alpha)P_{2n}(\cos\alpha)\,d\alpha \tag{4.6a}$$

or, for a uniaxial system as in our case:

$$\langle P_{2n}(\cos\alpha)\rangle = \int_0^{\pi/2} D(\alpha)P_{2n}(\cos\alpha)\sin\alpha\,d\alpha \tag{4.6b}$$

Wide-angle X-ray scattering technique has the ability to determine chain orientation in polymeric systems and give the complete orientation distribution function, $D(\alpha)$, through its harmonic component. It has been the practice to utilize the arcing in the WAXD pattern. For a fibre sample exhibiting a partial level of preferred orientation, the X-ray scattered intensity function, $I(Q,\alpha)$ can be written as the convolution of the scattering for a perfectly aligned system, $I^0(Q,\alpha)$, with the orientation distribution function $D(\alpha)$:

$$I(Q,\alpha) = I^0\left(Q,\alpha\right) * D(\alpha) \tag{4.7}$$

For cases in which each of these functions has uniaxial symmetry with an inversion center, the convolution may be written as [93-94]:

$$I_{2n}(Q) = I_{2n}^0(Q) D_{2n} \left\{ \frac{2\pi}{(4n+1)} \right\} \tag{4.8}$$

where $I_{2n}(Q)$, $I_{2n}^0(Q)$ and D_{2n} are the coefficients of a spherical harmonic expansion (see equation 4.4 and 4.6) of the functions $I(Q,\alpha)$, $I^0\left(Q,\alpha\right)$ and $D(\alpha)$. For example, $I_{2n}(Q)$ is given by [94]:

$$I_{2n}(Q) = (4n+1)\int_0^{\pi/2} I(Q,\alpha) P_{2n}(\cos\alpha) \sin\alpha \, d\alpha \tag{4.9}$$

with analogous definitions for $I_{2n}^0(Q)$ and D_{2n}. The complete scattering pattern may be calculated from :

$$I(Q,\alpha) = \sum_{n=0}^{\infty} I_{2n}(Q) P_{2n}(\cos\alpha) \tag{4.10}$$

or

$$I(Q,\alpha) = \sum_{n=0}^{\infty} \frac{2\pi}{4n+1} I_{2n}^0(Q) D_{2n} P_{2n}(\cos\alpha) \tag{4.11}$$

Thus in order to obtain values for the orientation parameter D_{2n} , we use the expression:

$$D_{2n} = \left(\frac{4n+1}{2\pi} \right) I_{2n}(Q) \big/ I_{2n}^{0}(Q) \tag{4.12}$$

It is more convenient to rewrite equation (4.12) in terms of the normalized amplitudes of the spherical harmonics:

$$\left\langle P_{2n}(\cos\alpha) \right\rangle_D = \frac{\left\langle P_{2n}(\cos\alpha) \right\rangle}{\left\langle P_{2n}(\cos\alpha) \right\rangle_0} \tag{4.13}$$

where $\left\langle P_{2n}(\cos\alpha) \right\rangle$, which must be normalized to be equivalent to equation 4.6(b) is given by :

$$\left\langle P_{2n}(\cos\alpha) \right\rangle = \frac{\int_0^{\pi/2} I(Q,\alpha) P_{2n}(\cos\alpha) \sin\alpha \, d\alpha}{\int_0^{\pi/2} I(Q,\alpha) \sin\alpha \, d\alpha} \tag{4.14}$$

The term of the right-hand side of equation 4.14 are sometimes abbreviated as $\left\langle I_{2n} \right\rangle$ and $\left\langle I_0 \right\rangle$ to give :

$$\left\langle P_{2n}(\cos\alpha) \right\rangle = \frac{\left\langle I_{2n} \right\rangle}{(4n+1) \times \left\langle I_0 \right\rangle} \tag{4.15}$$

and $\left\langle P_{2n}(\cos\alpha) \right\rangle_0$ is the amplitudes of the harmonics belonging to a model representing perfect alignment of molecules which appropriate to a crystalline array of regularly spaced and infinitely long molecules. For such an assemblage the interchain scattering is confined to the equatorial plane. This corresponds to the scattering taking the form of a delta-function and hence $I_{2n}^{0}(Q)$ components are given by:

$$\left\langle P_{2n}\left(\cos\alpha\right)\right\rangle_0 = \frac{(2n)!}{(-1)^n 2^{2n}(n!)^2} \tag{4.16}$$

The term $\left\langle P_{2n}\left(\cos\alpha\right)\right\rangle_0$ is sometimes abbreviated as P_{2n}^0 and the values for the first 4 terms are:

$$\begin{aligned} P_2^0 &= -\frac{1}{2} \\ P_4^0 &= \frac{3}{8} \\ P_6^0 &= -\frac{5}{16} \\ P_8^0 &= \frac{35}{128} \end{aligned} \tag{4.17}$$

Thus in practical terms, the measurement of orientaion using this approach reduces to the following stages.

1) Measure the azimuthal dependence of intensity $I(\alpha)$ at a scattering vector Q, corresponding to the maximum of this interchain peak.
2) Use equation 4.14 to evaluate $\left\langle P_{2n}\left(\cos\alpha\right)\right\rangle$.
3) Use the values given for P_{2n}^0 in equation 4.17 and equation 4.13 to give the orientation parameters $\left\langle P_{2n}(\cos\alpha)\right\rangle_D$

This relation yields the amplitudes of the even harmonics describing the distribution, which can be summed by equation 4.4 to give the full orientation distribution, $D(\alpha)$. Hence:

$$D\left(\alpha\right) = \sum_{n=0}^{\infty}\left(4n+1\right)\left\langle P_{2n}\left(\cos\alpha\right)\right\rangle_D P_{2n}\left(\cos\alpha\right) \tag{4.18}$$

The orientation description which was introduced above is given in references [95-96].

4.2.1.2 Small-angle X-ray scattering (SAXS)

Small-angle X-ray scattering (SAXS) is concerned with scattering phenomena occurring at small-angles. SAXS is used to obtain information on the periodicity of stacked lamellar crystals (long period) in semi-crystalline polymers, size and orientation of superstructures in the range of 1 – 100 nm. In SAXS patterns of fibres, there are two typical features, namely two-point pattern and four-point pattern, as represented in Fig. 4.9(a) and (b). The two-point pattern is due to the lamellae whose surface is perpendicular to the fibre axis as shown in fig. 4.9(a). For the four-point pattern, the lamellar surface is inclined with respect to the fibre axis (see Fig. 4.9(b)). The equatorial diffuse scattering in SAXS pattern is due to elongated scattering objects, such as micro-voids elongated parallel to the fibre axis. The interpretation of the equatorial scattering is more complicated since it may contain several contributions including the microfibrillar structure, voids morphology and the surface reflection/scattering of the fibre [97-98].

A SAXS pattern can be applied to provide more detail information about the morphology in the fibre, for example the lamellae layer thickness. Fig. 4.10 shows an arrangement of the crystal lamellae (parallel lines) with intervening amorphous regions as would be expected to occur in a fibrillar structure such as in a drawn fibre. The long period (d) includes one crystal thickness (l_c) and one amorphous interlayer thickness (l_a). This long period, d , which is the sum of l_a and l_c , can be approximately calculated from the peak position in the meridional scan (see Fig. 4.11) 醻 醼 醽 釀 釁 釛 針 釞 釺 ¥ ▯ ▯ ▯ £ ▯ £ ▯ £ 擇 ▯ e obtained from the expression:

$$l_c = d \times V_c \tag{4.19}$$

where V_c is the volume fraction of the crystalline component [11, 71].

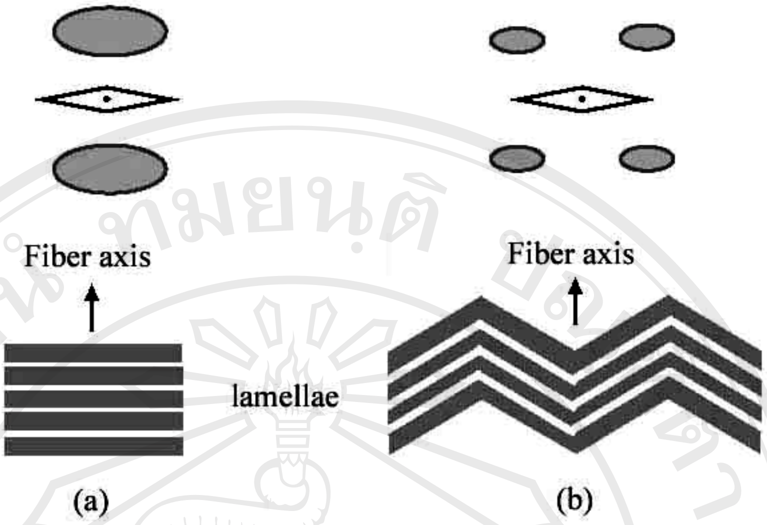

Fig.4.9 Typical SAXS patterns from fibres, (a) two-point pattern and (b) four-point pattern [11, 97].

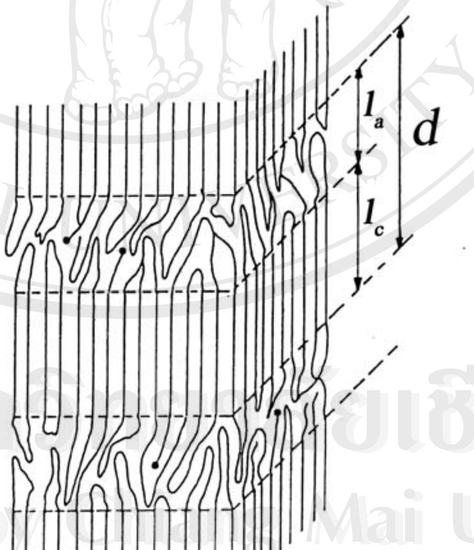

Fig. 4.10 Arrangement of the crystals and amorphous regions [71].

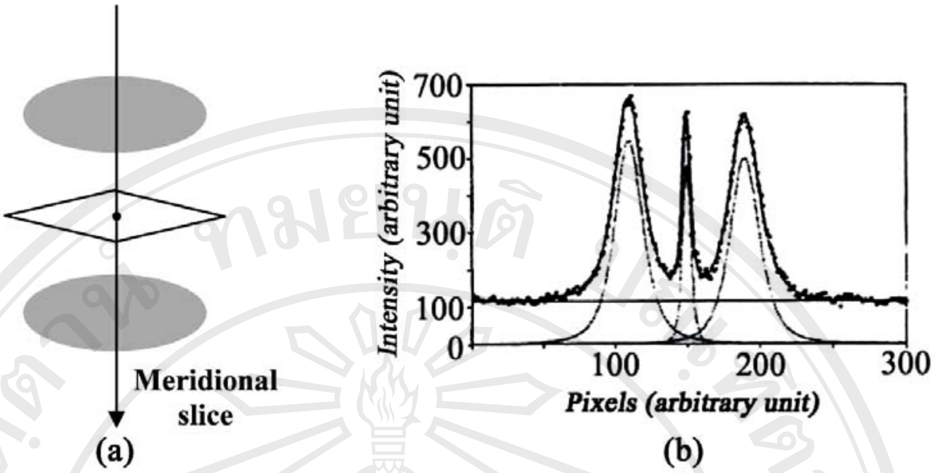

Fig. 4.11 (a) A schematic plot of a SAXS pattern with a meridional slice passing through the peak positions (b) A curve fitting profile to the intensity scan along a meridional slice as indicated by an arrow in (a) [97].

4.2.2 Microscopy

Microscopy permits magnification views of morphological structures to make details visible. Various techniques employed depend upon the level of magnification desired. Two techniques were used in this research work. One is optical microscopy (OM) which was employed to investigate morphology development of the polymers as discussed in section 4.3.3. The other is scanning electron microscopy (SEM) to provide images of fibres in more details as discussed in section 5.5. These two techniques are described below.

4.2.2.1 Optical microscopy (OM)

Magnification of an object viewed through an optical microscope is obtained by two lens systems, referred to as the objective and the eyepiece. The objective generates a magnified real image of the specimen. The real image is further magnified by the eyepiece and a magnified real image is formed at the retina of the eye. The maximum magnification obtained by OM is about 2000X. OM can resolve objects in a specimen as small as 1 μm. One of the optical techniques that yields good-quality images of polymer crystals utilizes the incident-light-polarizing microscope. A polarized microscope is equipped with two crossed polarizers. The schematic of incident-light-polarizing microscope is shown in Fig. 4.12. Light is passed through a polarizer plate and falls incident to the sample by use of a beam-splitting prism. The polarizer has served to orient the electric vector of the light in a plane. With the specimen not in place, the beam is reflected from the mirrored slide surface and passes through the analyzer plate before reaching the observer. The analyzer is set to pass only light whose electric vector is at 90° to the orientation imposed by the polarizer. Thus, no light reaches the observer when the specimen is not in place. The specimen serves to rotate the electric vector. Hence, when the specimen is inserted, a component of light will pass through the analyzer and reach the observer. The specimen thus appears light against a dark background [11,78].

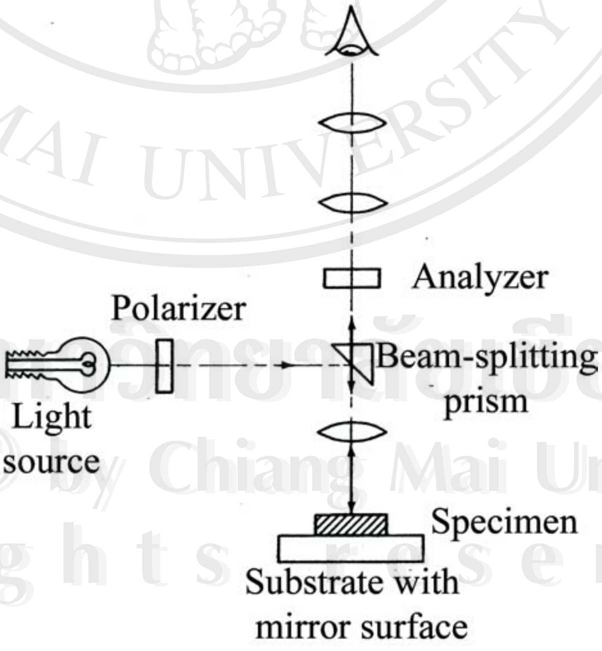

Fig. 4.12 Schematic representation of incident-light-polarizing microscope [78].

4.2.2.2 Scanning electron microscopy (SEM)

SEM produces detailed topographical images. It can resolve details smaller than 1 nm. A schematic diagram for a representative electron optical column of SEM is shown in Fig. 4.13. The electron gun at the top of the figure provides a source of electrons. Three condenser lens are used to demagnify the electron beam to a small spot about 5-50 nm in diameter from a crossover diameter more than a thousand times larger located inside the electron gun. The function of the final condenser lens is to move the smallest cross-section of the beam up and down until it meets the specimen surface. This corresponds to a focused image. Since electron beams are strongly absorbed or scattered by molecules in air, a high vacuum is essential in an SEM. Secondary electrons, which are emitted from the specimen with low energy, less than 50 eV are used to form an image. The double deflection coil, which are usually located inside the final condenser lens provide for deflection in both x and y directions across the specimen. As pictured in Fig. 4.13, the secondary emerging from a spot on specimen usually interacts with a scintillator producing light. The light is amplified by a photomultiplier tube (PMT) to produce an electrical signal that eventually modulates the intensity of the viewing in cathode-ray tube (CRT). This image is produced with great depth of field and an almost three-dimensional appearance. The specimens to be examined by SEM are coated with a thin layer of electrically conductive material such as gold [11, 13, 99-100].

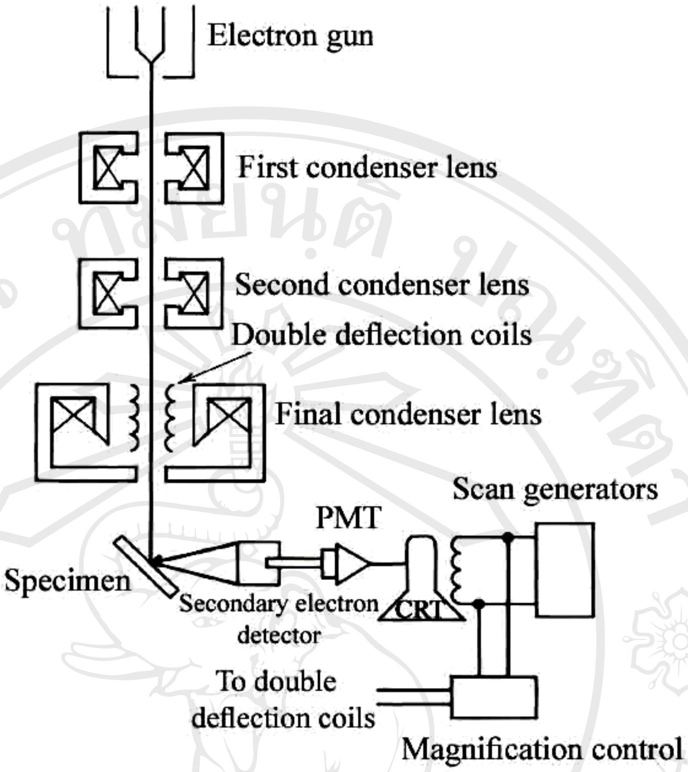

Fig. 4.13 Schematic diagram of part of the electron optical column of an SEM [99-100].

4.3 Polymer crystallization

4.3.1 Crystallization from a quiescent melt

Information of crystallization can be studied by using WAXS techniques. In this experiment, WAXS data were measured using a specially developed X-ray diffraction instrument called a 3-circle X-ray diffractometer. This is a symmetrical transmission diffractometer equipped with a graphite monochromator with pinhole collimation and a Cu K_α source. The geometry of the 3-circle X-ray diffractometer used in this experiment is shown in Fig. 4.14. The angle α is measured between fibre axis and scattering vector, $\boldsymbol{Q}$, where $\boldsymbol{Q} = 4\pi \sin\theta/\lambda$,2θ is the scattering angle and λ is the wavelength of the incident X-rays. Therefore the data collected at α = 90° is for the meridional section (parallel to the alignment axis or the fibre axis) and α = 0° is for the equatorial section (perpendicular to the alignment axis or the fibre axis). The X-ray source uses a Hilton Brookes generator operating at 40 kV and 20 mA with a Hilton Brookes shutter control [101].

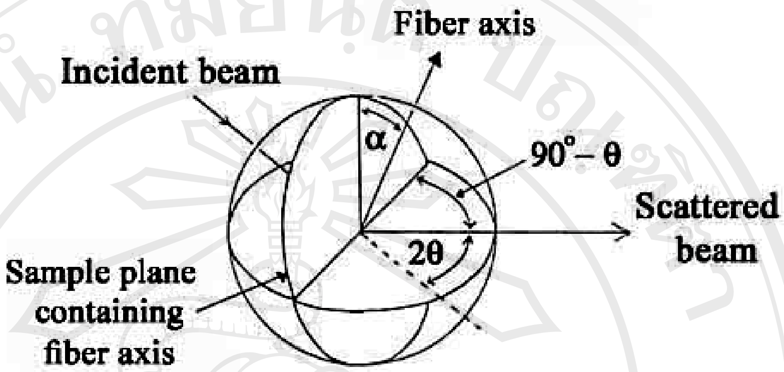

Fig. 4.14 Illustration of the geometry of the 3-circle X-ray diffractometer used in this experiment [94].

In this experiment, a polymer specimen was prepared prior to the scattering measurements by melting and then pressed into a thin film. The film was then mounted to cover a circular hole of 5 mm diameter of an aluminum plate and centred at the specimen position in the diffractometer. The intensity scattering from the specimen was then obtained as a function of $|\boldsymbol{Q}|$ over the range 0.2 to 6 Å^{-1} in steps of 0.02 Å^{-1}. Fig. 4.15 shows the intensity profiles obtained from poly(L-lactide), the random and block terpolymers.

All three intensity profiles exhibit both sharp and broad peaks typical of a semi-crystalline polymer. As can be seen clearly in Fig. 4.15, the three patterns show considerable similarity. The data for poly(L-lactide) has substantial peaks at $|\boldsymbol{Q}|$ ~ 1.12, 1.28, 1.98 and 2.2 Å^{-1}, while that for the random terpolymer shows peaks at $|\boldsymbol{Q}|$ ~ 1.16, 1.32 and 2.14 Å^{-1} and at $|\boldsymbol{Q}|$ ~ 1.14, 1.30, and 2.14 Å^{-1} for the block. It is not surprising that the sharp peaks in the patterns of the two terpolymers are somewhat broader and relatively less intense than the similarly positioned peaks for poly(L-lactide) due to their irregularity along the polymer chains.

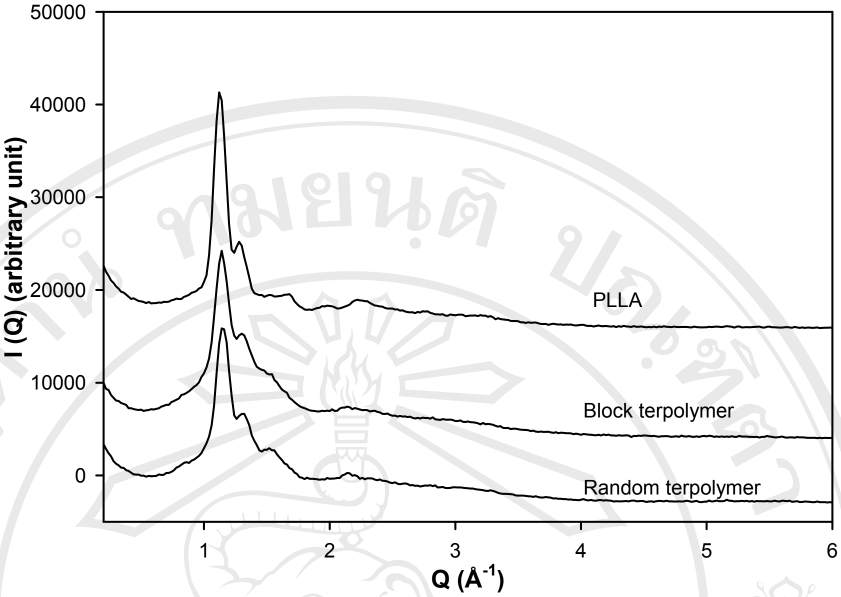

Fig. 4.15 Plots of the experimental wide-angle X-ray scattering intensity I(Q) recorded for samples of poly(L-lactide), the random and block terpolymers crystallized from a quiescent melt.

4.3.2 Rate of crystallization and fraction of crystallinity

In order to investigate the crystallization behavior of the two terpolymers in more detail, it was carried out isothermal crystallization at a series of temperature and used wide-angle X-ray scattering techniques to evaluate the rate of crystallization and the level of crystallinity. The 4-circle X-ray diffractometer equipped with a graphite monochromator, pinhole collimation and a CuK$_\alpha$ source of a Philips generator operating at 40 kV and 40 mA with Philips shutter control was used. The sample holder at the X-ray diffractometer was developed to contain a heating chamber for mounting a 2 mm diameter Lindemann glass capillary which allowed the temperature to be controlled within ±1°C.

In this experiment, as-spun fibres of random and block terpolymers were used to study natural rate of crystallization at various temperatures without inducement of crystallization by any drawing process. Since the as-spun fibres used were previously fabricated by melt-spinning and then quenching into cooled water. These as-spun fibres were almost completely amorphous. However, they might contain some crystallinity occurred during storage. They were then remelted and quenched in order to destroy any crystalline structure in the samples before investigating crystallization rate. Therefore, a sample of as-spun fibre was first cut into pieces and filled in a Lindemann glass capillary. The sample was then melted at 155°C for random and 165°C for block terpolymer and quenched rapidly in iced water. The X-ray scattering intensities from the quenched samples recorded as a function of $|\boldsymbol{Q}|$ from 0.5 to 3.5 $Å^{-1}$ in step of $\Delta\boldsymbol{Q}$ = 0.02 $Å^{-1}$ showed only diffused scattering with no any sharp crystalline peaks. This confirmed that both random and block terpolymers quenched samples were completely non-crystalline. These samples were then used to study rate of crystallization and fraction of crystallinity as described below.

The heating chamber for sample holder was preheated to the selected temperature, chosen in the range of T_g to T_m (40-135°C for both terpolymers). After the heating chamber's temperature appeared constant, each sample in a capillary was heated to remelt, quenched agained and then rapidly dropped into the chamber. The wide-angle X-ray scattering data were immediately collected to follow the nature of the crystallization process. A series of short scans centered at the peak position of $|\boldsymbol{Q}|$ = 1.18 $Å^{-1}$ were taken on a continuous basis to monitor the development of a crystalline structure, i.e. the peak intensity was recorded as a function of time. (Prior to the experiment, the peak position of the crystal structure was searched by scanning along $\boldsymbol{Q}$ from 0.02 to 2.0 $Å^{-1}$ and found to be at $|\boldsymbol{Q}|$ = 1.18 $Å^{-1}$ for 4-circle X-ray diffractmeter.) Fig. 4.16(a) shows as an example of peak intensity variation at $|\boldsymbol{Q}|$=1.18 $Å^{-1}$ as a function of time of the random terpolymer heated at 50°C.

After crystallization was completed (the peak intensity became constant with time), scattering intensities were recorded as a function of $|\boldsymbol{Q}|$ from 0.2 to 6.0 $Å^{-1}$ in step of $\Delta\boldsymbol{Q}$ = 0.02 $Å^{-1}$. Fig. 4.17 shows the scattering intensity profile obtained for the random terpolymer completely crystallized at 50°C. The crystallinity in the sample was then estimated by separating the crystalline and non-crystalline components of the wide-angle scattering data using standard non-linear least squares peak-fitting procedures in the region of $|\boldsymbol{Q}|$ from 0.5 to 2.0 $Å^{-1}$, as shown in Fig. 4.17. The fraction of crystallinity was calculated from the ratio of the $\boldsymbol{Q}^2$ weighted integral of the crystalline peaks to the equivalent integral for the total scattering [81] and shown in Table 4.1.

The crystallization rate for each particular isothermal crystallization temperature was then able to be evaluated. First, the peak intensity values on the curve in Fig. 4.16(a) were converted to be on a relative scale from 0 to 1.0 as replotted in Fig. 4.16(b). This is because that, at the beginning of the curve, its crystallinity corresponded to zero, while at the plateau of the curve at the end, it indicated maximum crystallinity was reached. Hence, the relative scale needed to subsequently be converted again to the scale of fraction of crystallinity, using its final fraction of crystallinity from Table 4.1, as shown in Fig. 4.16(b). The slope of this curve at the inflection point could be simply estimated as the rate of crystallization. The estimated rates of crystallization found for all chosen isothermal crystallization temperatures are shown in Table 4.1.

Fig. 4.18(a) shows a plot of rate of crystallization for a range of isothermal crystallization temperatures for the two terpolymers. These data reveals the typical bell-shaped curve with a maximum crystallization rate for the random terpolymer at ~ 90°C and for the block terpolymer at 100ºC. Fig. 4.18(b) shows a plot of the final fraction of crystallinity in the sample as a function of temperature. Over the temperature range from 50 to 120°C, the fraction of crystallinity lies in the range of 10-25%. It can be seen that the random terpolymer exhibits maximum crystallinity of slightly higher level at a lower temperature.

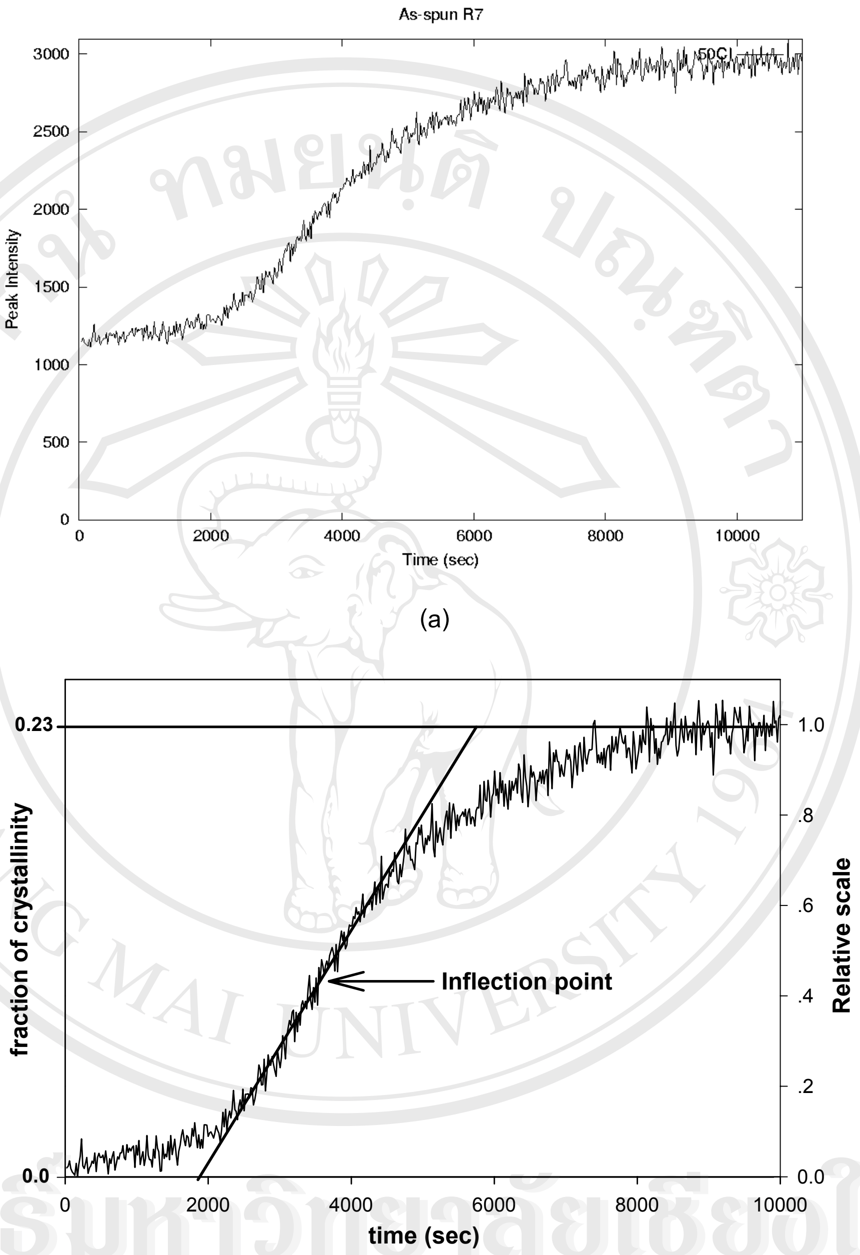

(a)

(b)

Fig. 4.16 (a) X-ray scattering intensity variation at $|\boldsymbol{Q}|$=1.18 Å^{-1}as a function of time of the random terpolymer heated at 50°C (b) fraction of crystallinity as a function of time calculated from (a) (see text); its slope at the inflection point indicates the rate of crystallization.

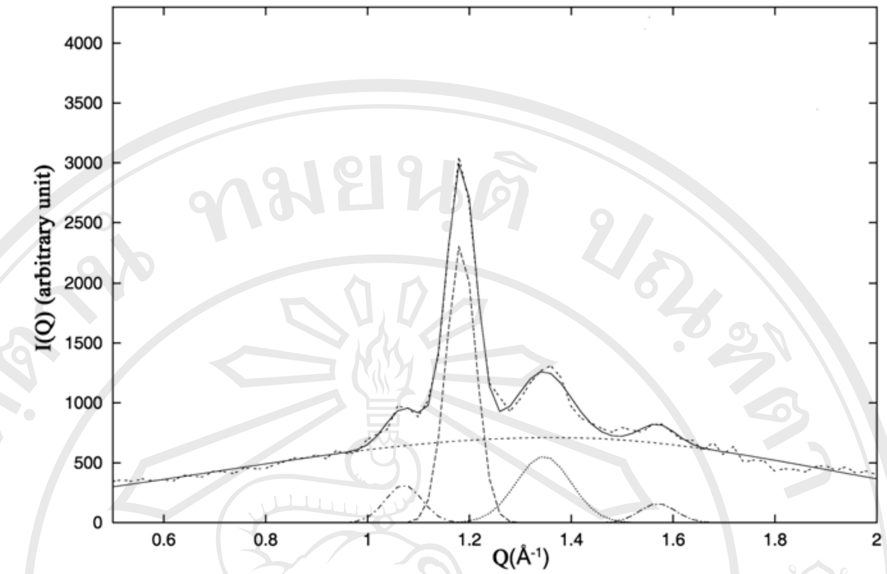

Fig. 4.17 Curve fitting to separate crystalline and amorphous scattering intensities for the random terpolymer completely crystallized at 50°C(see text)

Table 4.1 Rate of crystallization of the random and block terpolymers at various temperatures and final fraction of crystallinity.

Temperature (°C)	**Random terpolymer**		**Block terpolymer**	
	Rate of crystallization (× 10^3 sec^{-1})	**Final fraction of crystallinity**	**Rate of crystallization (× 10^3 sec^{-1})**	**Final fraction of crystallinity**
40	*	0.04	*	0.10
45	0.01	0.18	*	0.13
50	0.07	0.23	0.01	0.14
55	0.06	0.21	0.13	0.16
65	0.23	0.21	0.76	0.21
75	0.77	0.22	0.90	0.20
85	1.59	0.19	-	-
90	-	-	1.77	0.20
95	1.41	0.17	2.97	0.21
100	1.24	0.19	-	-
105	-	-	2.03	0.19
110	0.74	0.17	-	-
115	0.48	0.17	1.45	0.17
125	0.08	0.08	-	-
135	0.01	0.03	0.06	0.14

* Unable to determine

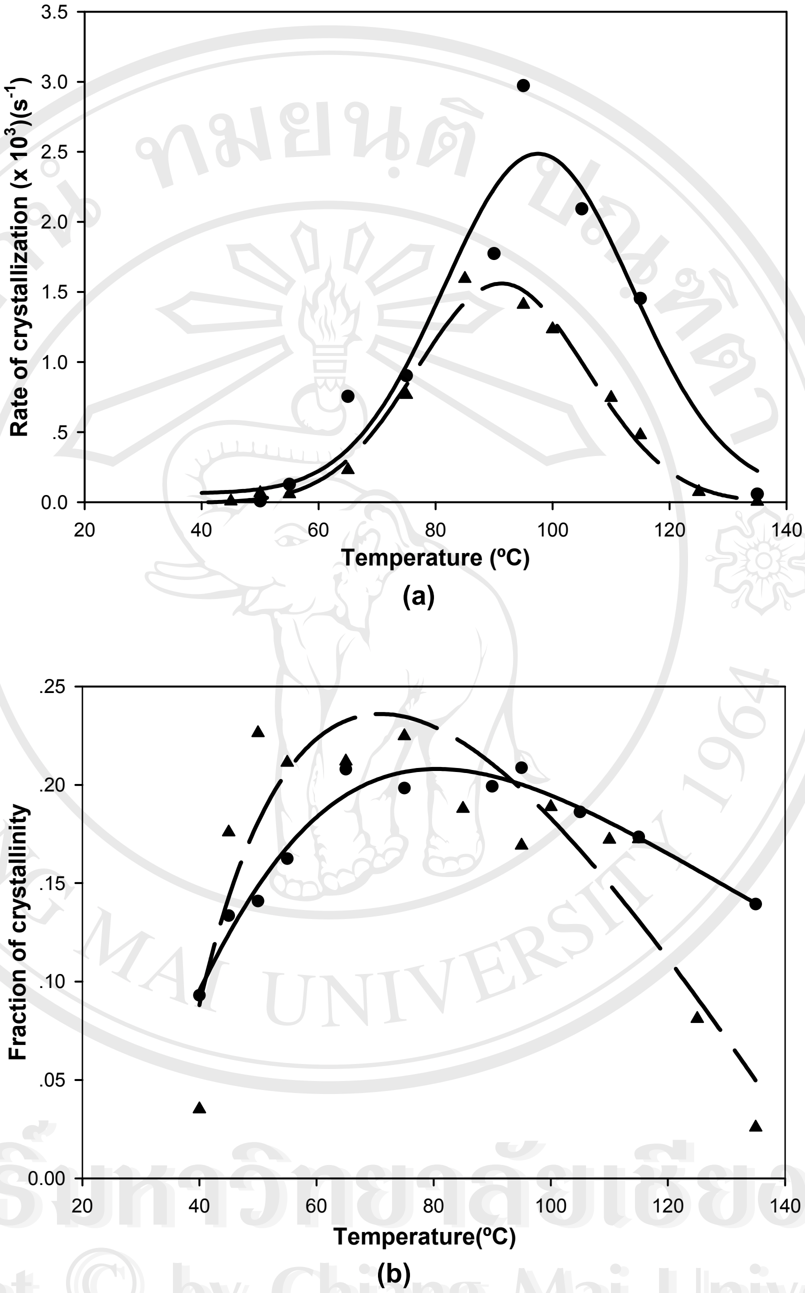

(a)

(b)

Fig. 4.18 (a) A plot of the rate of crystallization as a function of the isothermal crystallization temperature for the random terpolymer (▲, dashed-line) and the block terpolymer (•, full line) (b) a plot of the final fraction of crystallinity in samples of the random terpolymer (▲,dashed-line) and the block terpolymer (•, full line) as a function of the isothermal crystallization temperature.

4.3.3. Morphology development

The morphology of thin films of the terpolymers was investigated using a Swift-Bassett polarizing microscope equipped with a Mettler-Toledo programmable hot stage. The thin films were prepared by melting and pressing a small quantity of the terpolymers and poly(L-lactide) between two glass slides on a hot bar. Specimens were cooled at 20 °C/min from the melt and then, isothermally crystallized at the selected temperature (T_m- 40°C). Polarizing optical micrographs of thin films of the three samples are illustrated in Fig. 4.19. It can be seen that all the three samples cooled from the melt showed well defined spherulites and exhibited a strong, birefringent scattering texture. In addition, the terpolymers revealed a distinctive banded spherulitic structure (Fig. 4.19) with spherulite diameters of ~ 70-140 μm. Poly(L-lactide) crystallized under equivalent conditions exhibited non-banded spherulites. The observation of the banded spherulites in the case of the terpolymers and not in the homopolymer serves to underline the basic precepts of the banded spherulite model proposed by Bassett et al. [102].

Three specimens were then remelted and recrystallized under the same conditions as in the previous experiment to investigate crystallization behavior. Optical micrographs were recorded with time during isothermal crystallization, as shown in Figs. 4.20 – 4.22. The spherulite radii of the three polymers increased with time differently. Fig. 4.23 shows plots of averaged spherulite radius as a function of time for the terpolymers. Radial growth rate of spherulites of both terpolymers can be determined from the slope of the curve in Fig. 4.23.

Optical microscopy studies during crystallization reveal typical linear spherulite growth rate as shown in Fig. 4.23. It is clear that the spherulite growth rate of the block terpolymer is about twice that of the random terpolymer at the equivalent quench step below the melting point. This result agrees very well with that found by the WAXD techniques (see Table 4.1 and Fig. 4.18(a)). The growth rate is both a function of the composition and the sequence distribution as well as the molecular weight. As the homopolymer studied here has a different molecular weight to both block and random terpolymers, we have plotted in Fig. 4.24 the radial growth rate observed at a temperature corresponding to a constant degree of under cooling of (T_m– 40)°C for the three polymers produced in this study as a function of molecular weight along with some additional data for poly(L-lactide)s of different molecular weights taken from the literature [103-105]. The growth rates for the two terpolymers fall substantially below the fitted line for the poly(L-lactide). Clearly the chemical microstructure of the terpolymers has greatly reduced both growth rates with the random terpolymer being the most affected.

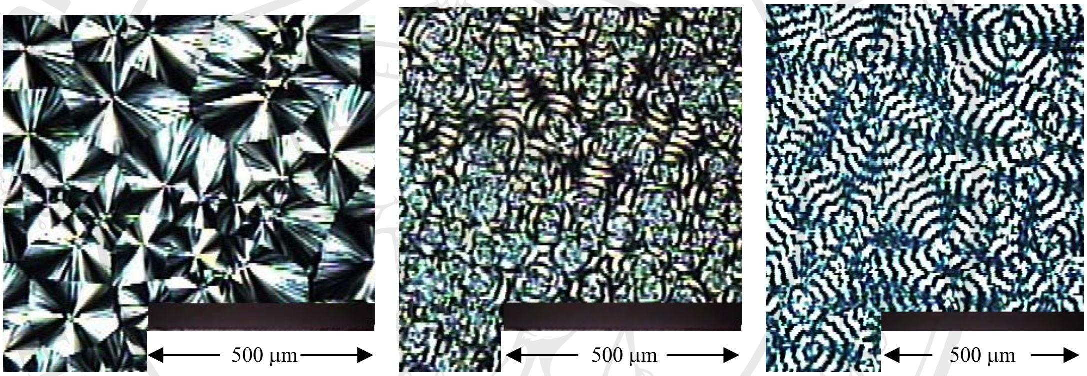

(a) (b) (c)

Fig. 4.19 Polarizing optical micrographs of thin films at room temperature after crystallization at (a) 130°C, poly(L-lactide); (b) 110°C random terpolymer and (c) 120°C block terpolymer showing well defined spherulites which for (b) and (c) are strongly banded.

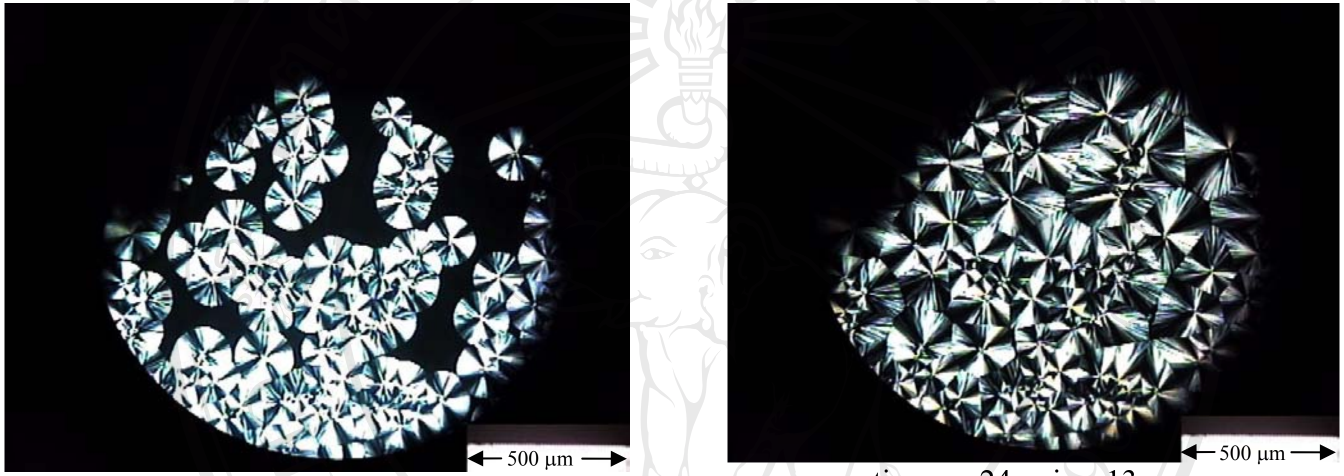

time = 11 mins 22 sec

time = 24 mins 13 sec

Fig. 4.20 Polarizing optical micrographs of poly(L-lactide) crystallizing at 130°C at different times from the melt.

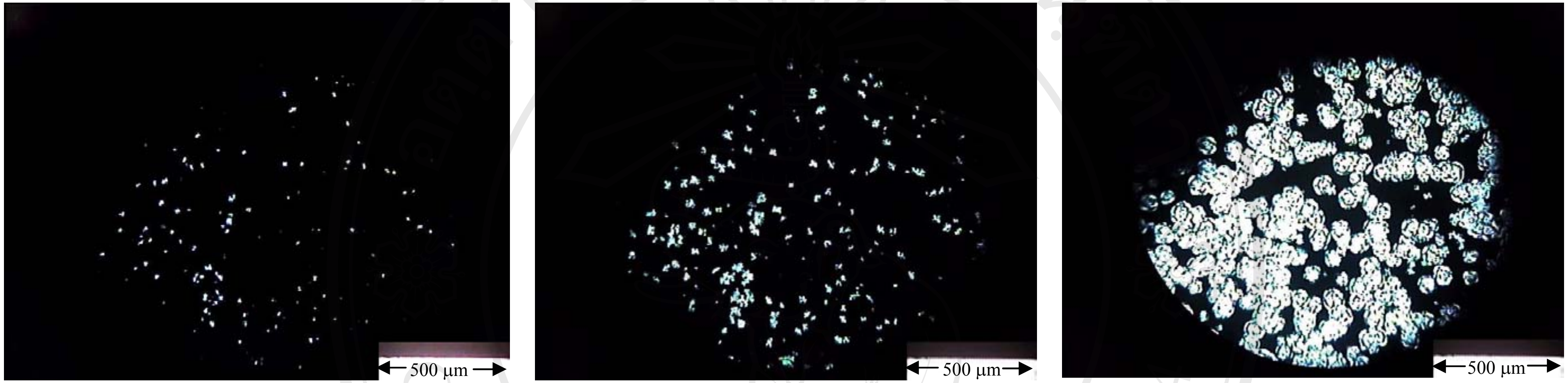

time = 11 min 22 sec time = 18 min 43.8 sec time = 42 min 12 sec

time = 58 min 12 sec time = 82 min

Fig. 4.21 Polarizing optical micrographs of the random terpolymer crystallizing at 110°C at different times from the melt.

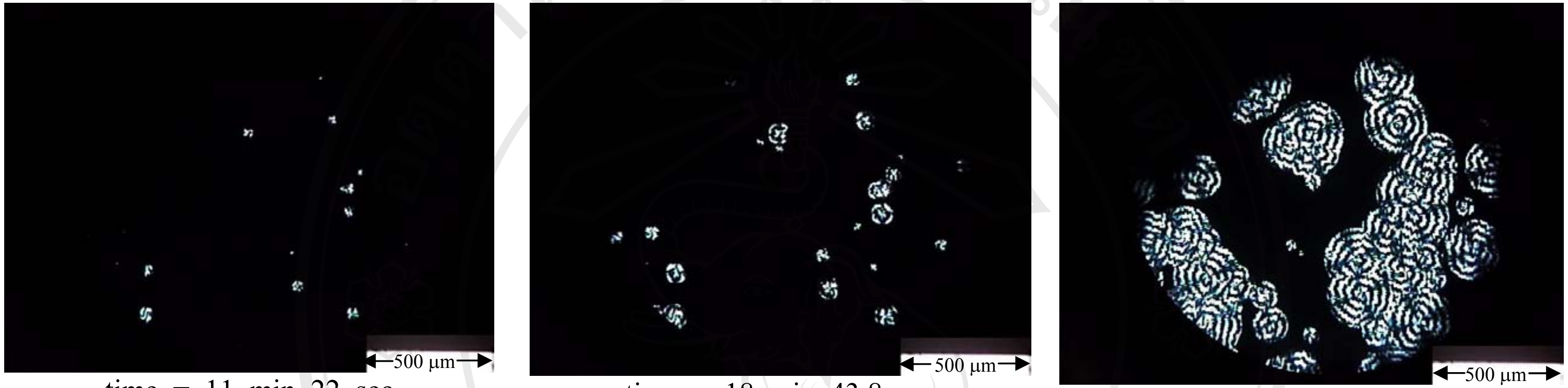

time = 11 min 22 sec

time = 18 min 43.8 sec

time = 51 min 28.2 sec

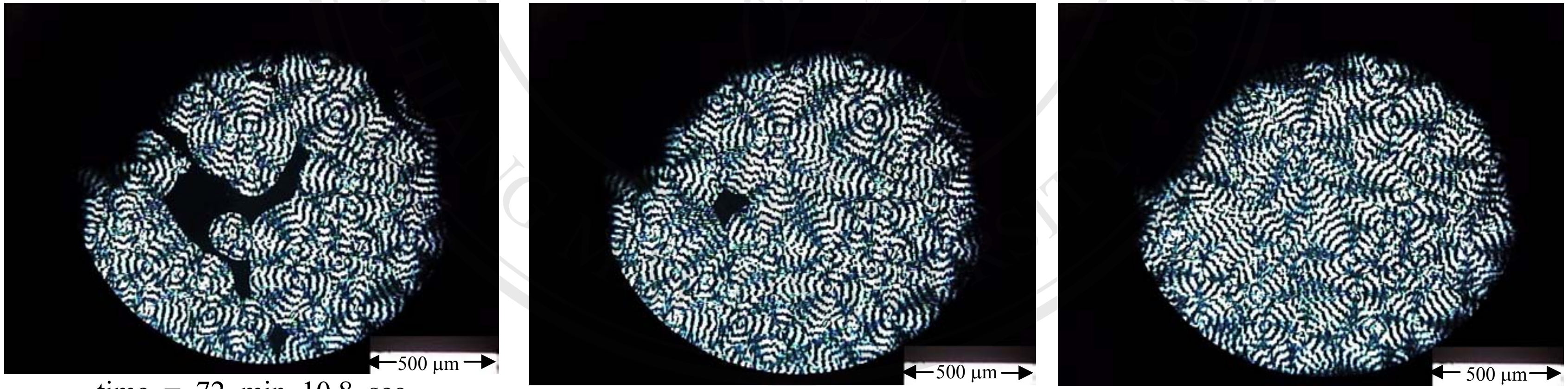

time = 72 min 10.8 sec

time = 91 min 43.8 sec

time = 106 min 42 sec

Fig. 4.22 Polarizing optical micrographs of the block terpolymer crystallizing at 120°C at different times from the melt.

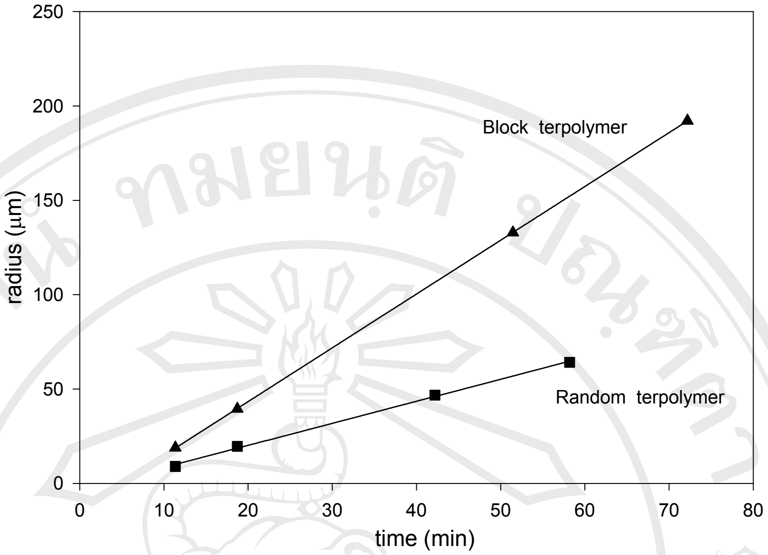

Fig. 4.23 Plots of radius of growing spherulites as a function of time for thin films of the random (at 110°C) and block (at 120°C) terpolymers after quenching from the melt.

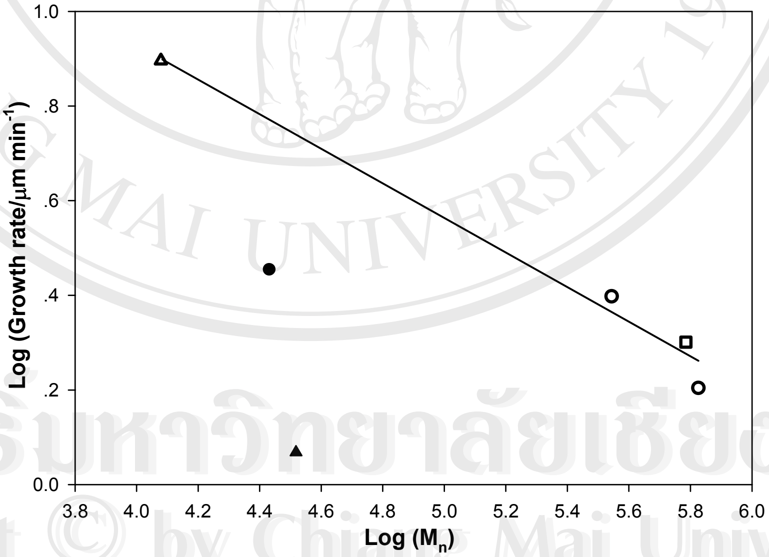

Fig. 4.24 A plot of the radial growth of spherulites against the molecular weight (Mn) for ▲ random terpolymer, ● block terpolymer and Δ poly(L-lactide) prepared in this work together with data for poly(L-lactide) taken from Ref. [104] (○) and Ref. [105] (□). The growth rates were measured at a constant degree of under cooling of ~ 40°C. The line represents a fit to the poly(L-lactide) data on the basis of a simple power law relationship between growth rate and molecular weight.

4.4 Structure of fibres

In order to obtain more details of the structure of the crystalline components in the fibres, use was made of maps of wide and small-angle X-ray scattering data (WAXS and SAXS data) obtained from fibres of the three polymers. The fibres used for the experiments were prepared under two distinct conditions, i.e.,

1. Hot-drawing to a high draw ratio and followed by annealing
2. Hot-drawing to a low draw ratio without annealing.

The structures of these fibres were then studied as described in the following sections.

4.4.1 Structure of hot-drawn fibres with annealing

This section was aimed to identify crystal structure in the terpolymer fibres. However, semi-crystalline polymer material normally gives rather diffused scattering of WAXD patterns due to its low crystallinity and high degree of disorder. To make the structure analysis possible for the terpolymer fibres, it was necessary to enhance crystallinity and its orientation in the fibres by drawing to a high draw ratio and follwed by annealing. Conditions for drawing and annealing the fibres for the structure analysis as described in this section are shown in Table 3.3.

WAXD patterns

2D WAXD patterns were collected using a 3-circle X-ray diffractometer as described in section 4.3.1. The specimens were prepared by mounting fibres in a close packed parallel array to cover a circular hole of 5 mm diameter of an aluminum plate as shown in Fig. 4.25. Typically, the X-ray beam samples 2-3 fibres.

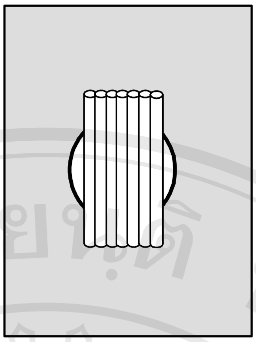

Fig. 4.25 Specimen for scattering measurement.

The intensity maps, $I(Q,\alpha)$, of WAXD patterns were obtained from data recorded both as a function of $|\boldsymbol{Q}|$ over the range 0.2 to 6 Å^{-1} in steps of 0.02 Å^{-1}and of α, over the range 0° to 90° in steps of 2°. The scattering data were corrected for the effects of absorption, polarization, multiple and incoherent scattering and scaled to absolute units using standard procedures [95]. Fig. 4.26 shows the X-ray scattering intensity maps for hot-drawn fibres of the three polymers.

All the maps show traditional X-ray scattering characteristic of fibre patterns. It is to emphasize that these are true undistorted reciprocal space maps of the scattering intensity. The vertical or meridional axis is a parallel to the fibre axis and is the axis of cylindrical symmetry. The horizontal or equatorial axis lies normal to the fibre axis. The point marked 0, 0 would correspond to the central part of a traditional fibre pattern. All three fibres exhibit a high level of preferred orientation such that in all three patterns it is possible to identify the layer line structure associated with a single crystal type texture with rotational symmetry about the fibre axis. There is clearly considerable similarity between the patterns. In Fig. 4.26, the accompanying sections also show the intensity along the equatorial and meridional sections. As seen in these sections, their intensity profiles are similar.

It was reported in the recent papers [83,87,106] that poly(L-lactide) could crystallize into different crystal forms depending upon the preparation condition. Three crystal forms have been observed for poly(L-lactide). The most common form exhibits an orthorhombic unit cell (a = 10.7 Å, b = 6.45 Å and c = 27.8 Å) in which the molecules adopt a -10/3 helical conformation, called α-phase [106]. Hoogsteens et al. [83] and Puiggali et al. [87] found that by adjusting the fibre processing conditions, two other forms might be observed. One of these is called β-phase which exhibits an orthorhomobic unit cell (a = 10.31 Å, b = 18.21 Å and c = 9.00 Å) in which the molecules possess a -3/1 helical conformation. The other is called γ-phase which appeared as frustrated packing of 3 fold helices within a trigonal unit cell with a = b = 10.52 Å and c = 8.8 Å.

By examining closely the WAXD patterns, the basic features observed in Fig. 4.26(a) match those reported for the α-phase of poly(L-lactide) both in terms of the position and intensity distributions of the meridional (c repeat) and the hk0 equatorial reflections. Fig. 4.27(a) shows a plot of horizontal sections of the data shown in Fig. 4.26(a) taken at regular intervals of 2π/c (c is for the α-phase of poly(L-lactide)) corresponding to the so-called layer lines on which scattering intensity is confined for a uniaxial fibre. As expected for the α-phase, the first layer line with intensity peak on the meridian corresponds to the 10th layer. By comparison of the intensity distribution along each of these layer lines to the equivalent functions calculated for the α crystal structure [88], there is excellent correspondence between observed and calculated values confirming the presence of the α-phase.

Fig. 4.26(b) shows the map of the scattered X-ray intensity for fibres of the random terpolymer. The equatorial section contains three peaks at $|\boldsymbol{Q}| \sim 1.16$, 1.52, and 2.00Å^{-1} and peaks at $|\boldsymbol{Q}| \sim 1.20$ and 2.14 Å^{-1} in the meridional section. The pattern has many features in common with that for the poly(L-lactide) although there is clearly a much larger non-crystalline component as can be seen from the diffuse isotropic scattering centered on $|\boldsymbol{Q}| \sim 1.2$ Å^{-1}. Although the structure is somewhat smeared, probably as a result of smaller crystals, it is clear that the pattern of intensity of the sharper crystalline features observed for the poly(L-lactide) are reproduced in the random terpolymer pattern. The positions of the hk0 reflections, the layer line spacing and the distribution of intensity along each layer line (Fig. 4.27(b)) are more or less equivalent between homopolymer and random terpolymer although the spacing of higher order hk0 reflections makes calculation of the unit cell for the latter rather imprecise. However, it is clear that the crystal structure is equivalent to the α-phase of poly(L-lactide).

A similar pattern of observations can be made with respect to the intensity map for the block terpolymer (Fig. 4.26(c)). The block terpolymer exhibits three peaks at $|\boldsymbol{Q}| \sim 1.16$, 1.52 and 1.98 on the equatorial section and two peaks ~ 1.30 and 2.14

Å^{-1}on the meridional axis. Again a comparison of the features including the layer line intensity distributions (Fig. 4.27(c)) confirms the presence of a crystal structure equivalent to the α-phase of poly(L-lactide). The strong equatorial feature at $|\boldsymbol{Q}| \sim$ 1.2 Å^{-1} which corresponds to the 110 peak in the α-phase and is present in all three fibre patterns has a breadth at half height of ~ 0.15 Å^{-1}. A similar breadth is observed for the 0,0,10 reflection on the meridian. This corresponds to crystal sizes of the order of 40 Å (= $\frac{2\pi}{\Delta Q}$ where ΔQ is the half-width of the peaks [109]), although we have not corrected for any instrumental broadening.

For the α-phase of poly(L-lactide), meridional reflections should be limited to the 10th, 20th etc. layer lines. A number of authors have reported the presence of meridional reflections on other layer lines, which they have interpreted as arising from non-integer helices and variation in the up-down symmetry of neighbouring chains [82-84,88]. For the poly(L-lactide) annealed fibre, some very weak scattering were observed on the 7th layer line on the meridional axis. However, as with Sasaki et al. [88] this is attributed this to streaking from nearby reflections on the same layer line. Other than a very weak reflection at ~ 4.30 Å $^{-1}$ corresponding to the 20th layer line, meridional reflections on any other layer lines were not observed in this work.

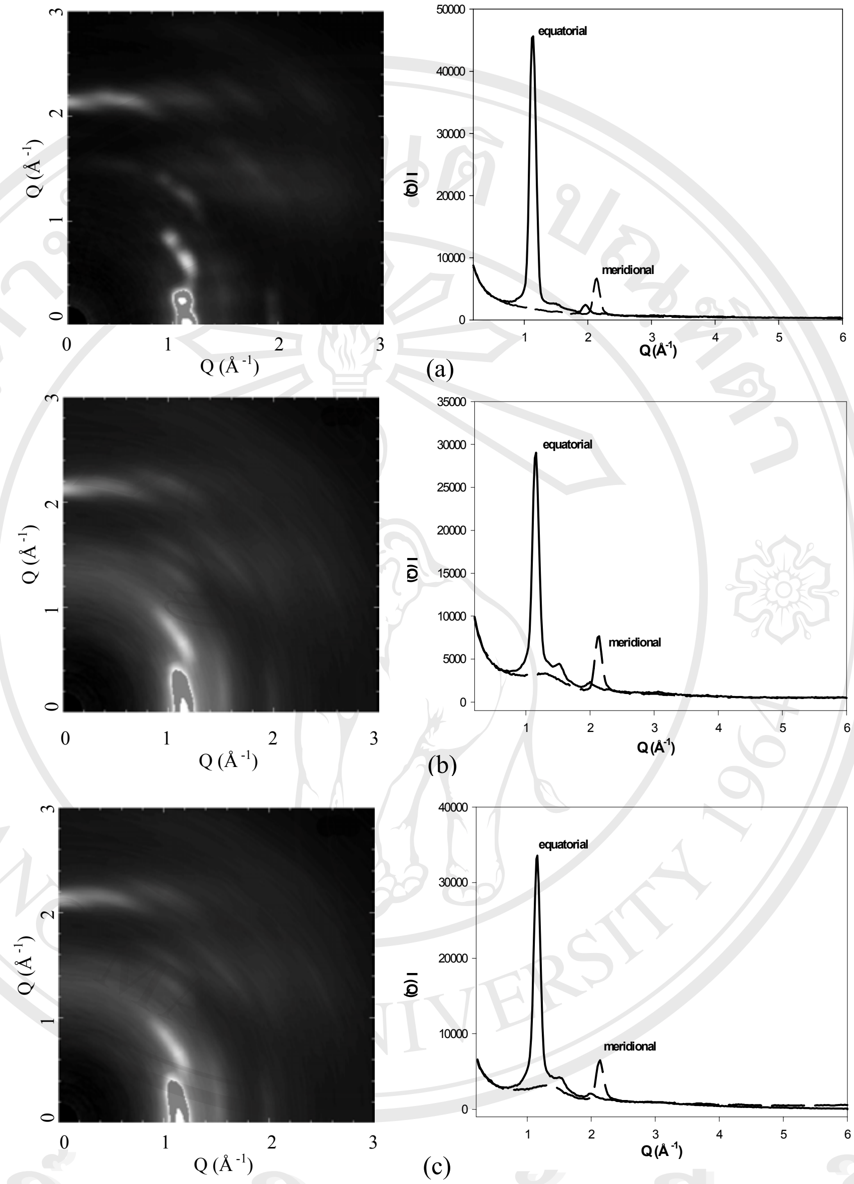

Fig. 4.26 X-ray scattering intensity maps $\boldsymbol{I}(\boldsymbol{Q},\boldsymbol{\alpha})$ for the annealed fibres of (a) poly(L-lactide), (b) random terpolymer and (c) block terpolymer. In each case the fibre axis is vertical. The grey scale representation is arranged to that white represents the highest intensity. Note that the grey scale has been truncated to allow the details within the pattern to be observed. The relative strength of the strong equatorial feature at $|\boldsymbol{Q}| \sim 1.2$Å^{-1} can be judged from the equatorial section. The accompanying line plots show the equatorial (α=0°, full line) and the meridional section (α=90°, broken line).

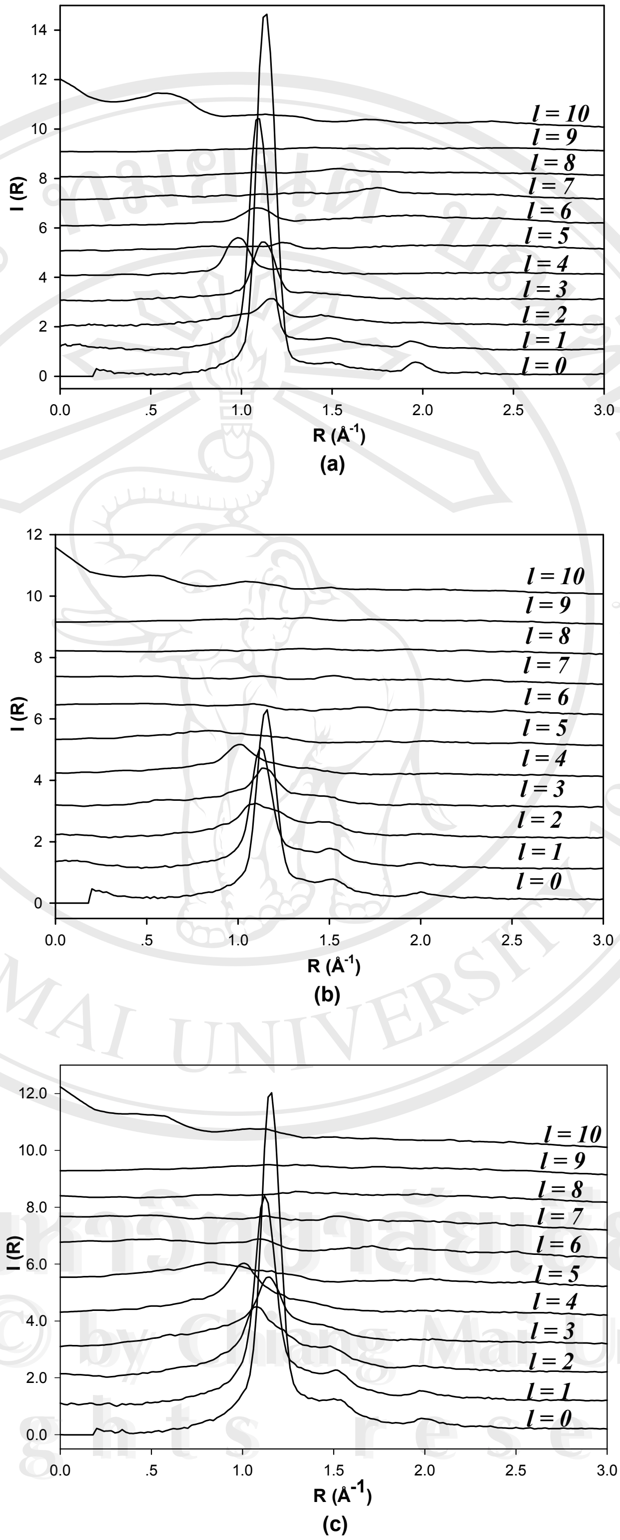

Fig. 4.27 Cross-sections of the intensity maps shown in Fig. 4.26 taken at constant Z values corresponding to the layer line number indicated in the figures ; (a) poly(L-lactide) (b) random terpolymer (c) block terpolymer.

SAXS patterns

For small-angle X-ray scattering, the experiments were performed on the fixed wavelength ($\lambda = 1.4$ Å) beam-line 16.1 at the Daresbury synchrotron radiation source (UK) using a beam ~ 0.3 mm diameter. SAXS data in the range $|\boldsymbol{Q}| \sim 0.01$ to 0.12 Å^{-1} were recorded using a 2-D RAPID detector with a data accumulation times of 10s. The intensity data were normalized to the incident beam using the values obtained from an ionization chamber prior to the sample. The SAXS detector was calibrated in terms of geometry using the scattering from a collagen sample obtained from a rat tail tendon mounted in place of the fibre samples.

The small-angle X-ray scattering patterns for the as-spun filaments of the random and block terpolymers are as shown in Figs. 4.28(a) and (b) show no distinctive features other than a small level of continuous scattering from simple density fluctuations. This suggests that the block terpolymer does not exhibit any microphase segregation in the melt. This is not surprising as there will be quite a broad distribution of the block lengths from one polymer chain to another. In contrast, the patterns recorded for the annealed fibres show very strong and highly anisotropic scattering features as shown in Fig. 4.29. For the random terpolymer (Fig. 4.29(a)), it shows very sharp meridional peaks indicating a highly aligned two phase structure. (The azimuthal variation of intensity is probably defined by the resolution of the instrument rather than any slight misorientation of the crystallites.) The peak position is 0.038 Å^{-1} and the peak width is 0.01Å^{-1}. There is also an equatorial streak, which probably arises from micro-voids in the original as-spun fibre, which have been extended during hot-drawing. The block terpolymer fibre shows a similar pattern but the scattering is very much weaker with maxima at 0.031 Å^{-1} and a peak width of 0.02 Å^{-1}.

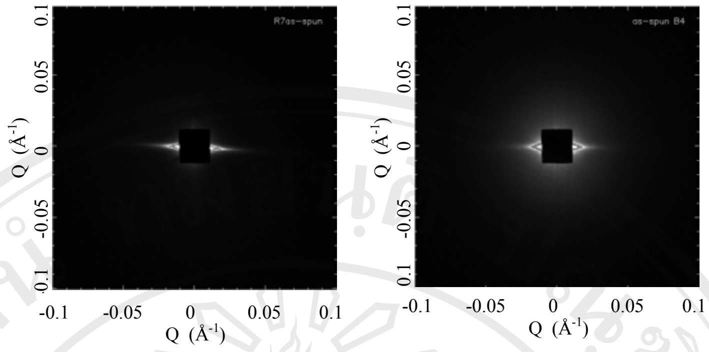

(a) (b)

Fig. 4.28 Small-angle X-ray scattering patterns recorded for as-spun fibres of (a) the random and (b) block terpolymers.

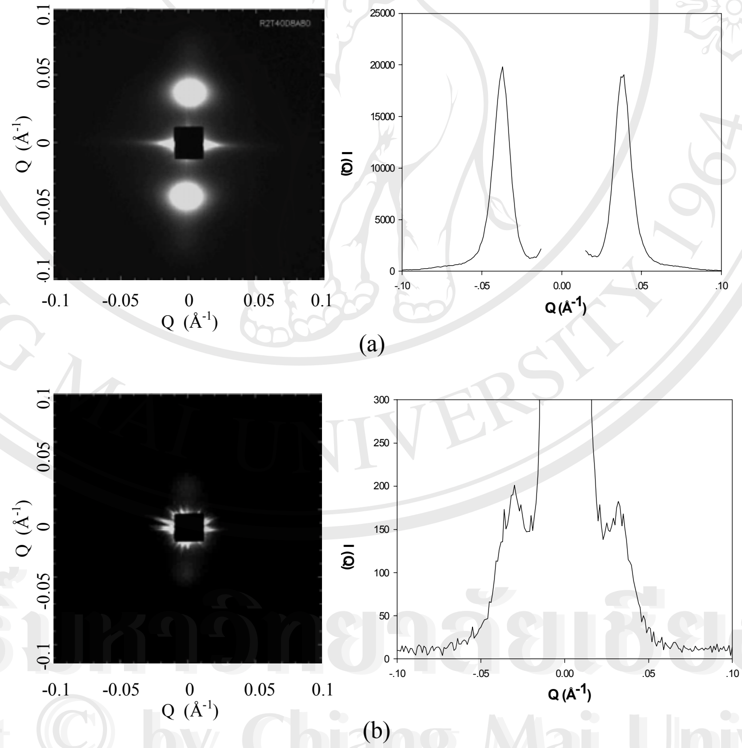

(a)

(b)

Fig. 4.29 Small-angle X-ray scattering patterns recorded for the same annealed fibres as in Fig. 4.26 i.e. (a) annealed random terpolymer and (b) annealed block terpolymer. In each case the fibre axis is vertical. The dark square in the centre is the shadow of the beam stop. In Fig. 4.29(b), the scattering is much weaker than in Fig. 4.29(a) and some scattering from the collimation system can be seen around the beam stop in the form of short spikes.

Calculation of long period and crystal size from SAXS data

As described in section 4.2.1.2, a SAXS pattern can be utilized to investigate morphology in a fibre, especially in a highly-aligned fibrillar structure. Fig. 4.29 provides excellent evidence for the differences of morphologies in both terpolymer fibres. From the peak positions along the meridional direction in the SAXS patterns for both random and block terpolymers, ($|Q|$ = 0.038 Å^{-1} and $|Q|$ = 0.031 Å^{-1} respectively), the corresponding long periods (d) are calculated from the equation below.

$$d = \frac{2\pi}{Q}$$

For the random terpolymer fibre ; $= \frac{2\pi}{0.038} \approx 160$ Å

For the block terpolymer fibre ; $= \frac{2\pi}{0.031} \approx 200$ Å

For the fibrillar structure such as that shown in Fig. 4.10, the long period includes one crystal thickness (l_c) and one amorphous interlayer (l_a). Such morphology model could reasonably be applied to our fibres since the SAXS patterns shown in Fig. 4.29 indicate clearly two-point pattern (see Fig. 4.9) The average crystal thickness (l_c) could therefore be calculated by equation 4.19 and V_c which is the fraction of crystallinity of the sample. The maximum crystallinities used were as shown in Table 4.1, i.e. V_c = 0.22 and 0.21 for the random and block terpolymers. The crystal thickness obtained for both terpolymers were found to be ~ 35 and 42 Å.

Discussion of structure of hot-drawn and annealed fibres from WAXS and SAXS measurements

The WAXS and SAXS data provides a detailed view of the multiple phase morphology. For both terpolymers, the crystallites are formed from the lactide units. There is no evidence for any crystal structure corresponding to that exhibited by poly(ε-caprolactone) [107]. The lactide units crystallize in a structure equivalent to the α-phase of poly(L-lactide). The block terpolymer crystallizes more rapidly presumably due to the greater mobility of the end blocks but the random terpolymer displays a highly developed lamellar stack type SAXS pattern, suggesting better defined crystals than in the block terpolymer system where the equivalent SAXS is rather weak. The SAXS patterns give long periods of the order of 160 Å for the random terpolymer and 200 Å for the block terpolymer. With crystallinity levels as recorded in Fig. 4.18(b), this suggests crystal sizes of 35 and 42 Å for the random and block terpolymer, respectively similar to those derived from the peaks in WAXD pattern (~ 40 Å). The lactide sequence in either the random or terpolymer determined by NMR is of the order of 10 (see section 2.6.5) which corresponds to 60 Å (that was calculated from the length of one L-lactide unit of ~ 6 Å [83]) for a chain in a -10/3 helix conformation.

4.4.2 Structure of hot-drawn fibres without annealing

Although the annealed fibre patterns provide an excellent basis for structural analysis, such fibres are unsuitable for use as absorbable sutures as they are too stiff due to their high level of crystallinity. The major required mechanical properties of absorbable surgical sutures are good tensile strength and flexibility. Such properties strongly relate to the fibre's morphology involving crystallinity and molecular orientation. To obtain suitable morphology for particular mechanical properties, the fibre processing needs to be carefully controlled under the decided drawing conditions such as draw temperature, draw rate and draw ratio. During the process of drawing, molecular orientation and crystallization are induced, as described in section 3.2. The fibres of the random and block terpolymers drawn under different conditions to low draw ratio at rather low draw temperature without annealing as described in Table 3.14 were expected to obtain suitable properties for sutures. This section will describe the way in which the structure in such drawn fibres without annealing can be investigated.

Fig. 4.30(a) and (b) show X-ray scattering patterns for the unannealed fibres of the random and block terpolymers respectively. The accompanying line plots in these figures are the intensity profiles along the equatorial and meridional sections. Comparison of these patterns with those for the annealed fibres (Fig. 4.26) reveals a greater extent of azimuthal arcing indicating a lower level of orientation. This serves to smear the features. We can identify an intense feature on the equatorial sections at $|\boldsymbol{Q}|$ = 1.16 Å^{-1} and a rather weaker meridional feature at $|\boldsymbol{Q}|$ =2.14 Å^{-1} in the pattern for the random terpolymer. The block terpolymer pattern exhibits an intense equatorial feature at $|\boldsymbol{Q}|$ = 1.16 Å^{-1} and a meridional feature at $|\boldsymbol{Q}|$ = 2.18 Å^{-1}. The breadth of the equatorial peak for the block terpolymer ($\Delta\boldsymbol{Q}$ = 0.34 Å^{-1}) is about twice that observed for the equivalent peak in the pattern for the random terpolymer. The breadths of the meridional features are $\Delta\boldsymbol{Q}$ = 0.31 Å^{-1} for the block terpolymer and $\Delta\boldsymbol{Q}$ = 0.25 Å^{-1} for the random terpolymer.

Comparison of the fibre patterns with the equivalent patterns recorded for the annealed fibres suggests that the structures are similar but clearly it is not possible to identify directly the well defined layer lines present as in Fig. 4.27. However, some information of the structure from these fibre patterns such as the orientation distribution function may be deduced. It has been employed a novel approach to the wide-angle X-ray scattering data as follows.

For a fibre sample exhibiting a partial level of preferred orientation such as these drawn fibres of the terpolymers, the scattering, $I(Q,\alpha)$, may be represented by a series of spherical harmonics, as described in section 4.2.1.1. The components of each series, $I_{2n}(Q)$, can be obtained by equation 4.9 and also shown below.

$$I_{2n}(Q) = (4n+1)\int_0^{\pi/2} I(Q,\alpha)P_{2n}(\cos\alpha)\sin\alpha\, d\alpha$$

By using the observed scattering data, $I(Q,\alpha)$, of the diffraction patterns of the polymers and a series of spherical harmonics $P_{2n}(\cos\alpha)$ as shown in equation 4.5, the components or amplitudes $I_{2n}(Q)$ for $n = 0, 1, 2, 3$ were evaluated and plotted as a function of Q for the annealed and unanneal samples of three polymers in Figs. 4.31 and 4.32 for further investigation as described below.

The use of this novel approach is that the effects of preferred orientation are separated from the dependence of the scattering on the spatial correlations [94, 108]. Equation 4.8 shows that for samples with the same structure, the variations of the amplitudes of the spherical harmonics $\boldsymbol{I}_{2n}(\boldsymbol{Q})$ with $\boldsymbol{Q}$ are essentially the same, with a simple constant multiplier dependent on the level of preferred orientation. The orthogonal nature of the spherical harmonics, in equation 4.8, means that for multiple phase structures as considered here, where the scattering from the different phases is additive, the resultant spherical harmonics will also be linear combinations of the harmonic functions for each phase.

To check the efficacy of this approach, a comparison is made of the first four components (see Fig. 4.31) of the series of spherical harmonics derived from the patterns shown in Fig. 4.26, i.e. the annealed fibres. The weight of any feature in a harmonic is a function of the fraction of the material which exhibits that structure and the level of preferred orientation as well as the relative strength of the underlying structure factor.

The spherical harmonics for $2\boldsymbol{n} > 0$ represent the anisotropic scattering and hence they will contain only the aligned crystalline and aligned non-crystalline scattering. If we compare the three curves each of Fig. 4.31(a)-(d) it is clear that each of the features (i.e. maxima and minima) observed in the appropriate spherical harmonic are reproduced in the equivalent functions derived from the scattering for the two terpolymers. The variations in height reflect the small differences in preferred orientation between the three fibre samples. The curves for $2\boldsymbol{n} = 0$ (Fig. 4.31(a)) show larger differences due to the variations in crystallinity between the three samples as reflected most clearly in the height of the sharp peak at $|\boldsymbol{Q}| = 1.18\text{Å}^{-1}$. Despite such differences in weightings, this can discern that the various features present in the poly(L-lactide) sample are also present in the equivalent curves for the two terpolymer fibres. These observations underpin the observations already made in section 4.4.1 using the complete patterns and the layer line plots. Clearly the method is effective and does not require any assumption about the orientation distribution function or numerical approximations.

Fig. 4.32 shows the first four spherical harmonic components derived from the scattering patterns shown in Fig. 4.30 compared to those derived from the scattering pattern of the poly(L-lactide) shown in Fig. 4.26(a). If the curves for $2\boldsymbol{n} > 0$ are considered it is clear that the features for the poly(L-lactide) are very much more intense than those observed in the curves relevant to the terpolymer fibres. This simply reflects the higher proportion of anisotropic material and the higher level of preferred orientation present in the poly(L-lactide) fibre. In terms of the key minima and maxima ($|\boldsymbol{Q}|$ = 1.18, 1.3 and 2.4 Å^{-1}), the curves are equivalent indicating that it is reasonable to conclude that the terpolymer filaments prepared at low draw ratios and without annealing exhibit a similar crystal structure to poly(L-lactide) despite the smaller crystal size and greater crystal misorientation.

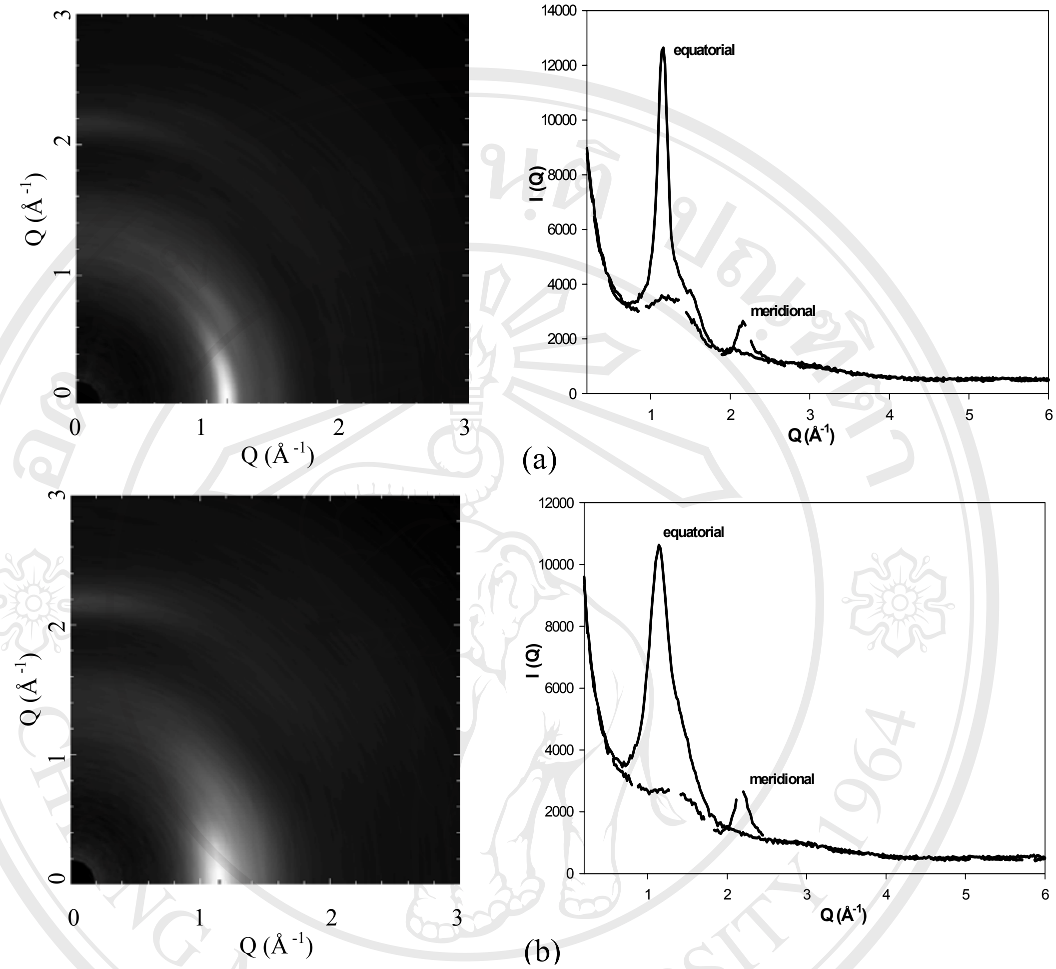

Fig. 4.30 X-ray scattering intensity maps $\boldsymbol{I(Q,\alpha)}$ for the unannealed fibres of (a) random and (b) block terpolymers. In each case the fibre axis is vertical. The grey scale representation is arranged to that white represents the highest intensity. Note that the grey scale has been truncated to allow the details within the pattern to be observed. The relative strength of the strong equatorial feature at $|\boldsymbol{Q}|$ ~ 1.2 Å^{-1} can be judged from the equatorial section. The accompanying line plots show the equatorial (α=0°, full line) and the meridional section (α=90°, broken line)

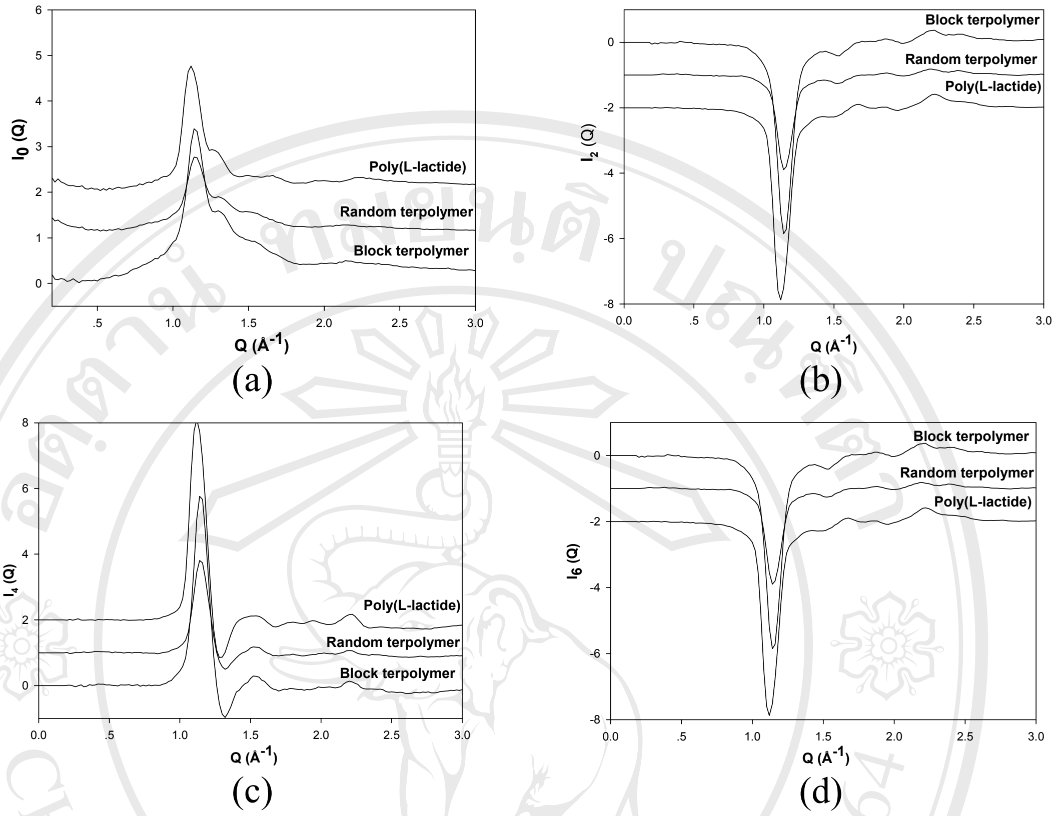

(a) (b)

(c) (d)

Fig. 4.31 A comparison of the amplitudes of the series of spherical harmonics which represent the fibre patterns shown in Fig. 4.26 for the annealed samples of the poly(L-lactide), the random and block terpolymers. Each curve has been offset for clarity but in all cases the value of the functions at $|\boldsymbol{Q}| = 0.0$ $Å^{-1}$ is zero.

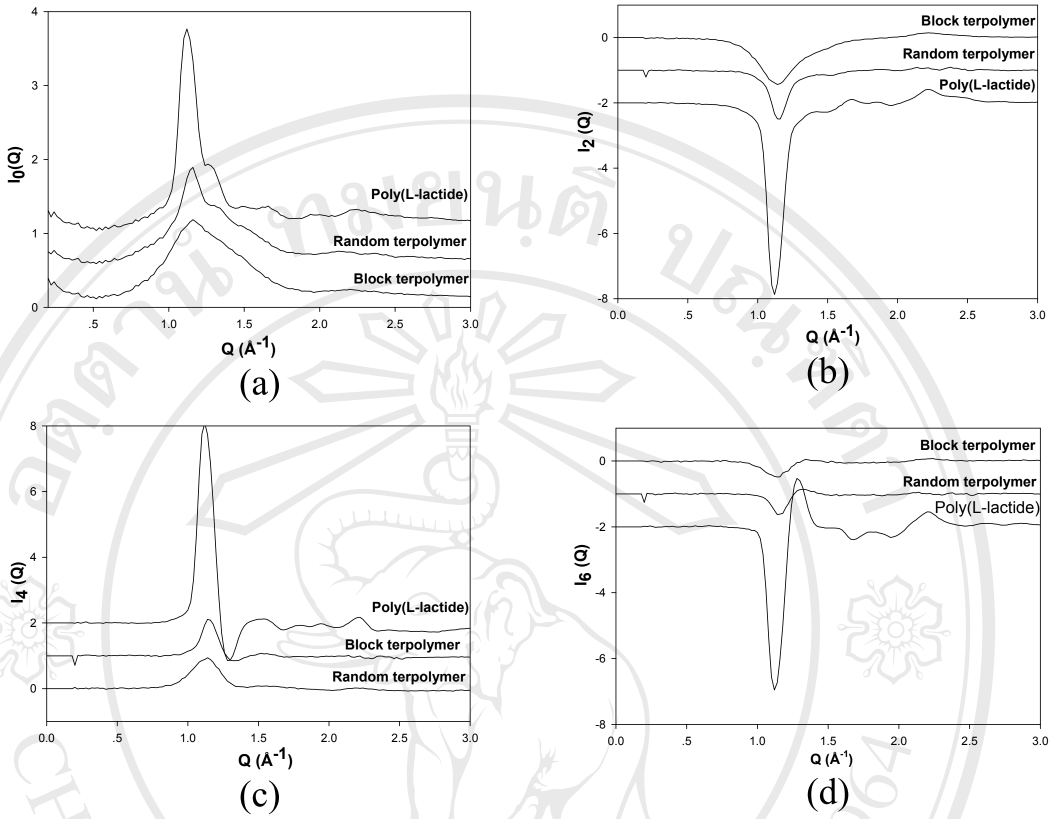

(a) (b) (c) (d)

Fig. 4.32 A comparison of the amplitudes of the series of spherical harmonics which represent the fibre patterns shown in Fig. 4.30 for the unannealed samples of the random and block terpolymers with those derived from the annealed poly(L-lactide) shown in Fig. 4.26.

4.4.3 Structure of undrawn fibres

In order to confirm that the drawing does not induce any changes to the crystal structure other than the level of preferred orientation and degree of crystallinity, samples of the three polymers crystallized from quiescent melts were prepared, as described in section 4.3.1 and their X-ray scattering intensity were recorded as a function of $\boldsymbol{Q}$ using the same diffractometer as employed to record the fibre scattering data. The fully corrected and scaled intensity functions, labeled as $\boldsymbol{I}(\boldsymbol{Q})$ isotropic sample, are shown in Fig. 4.33.

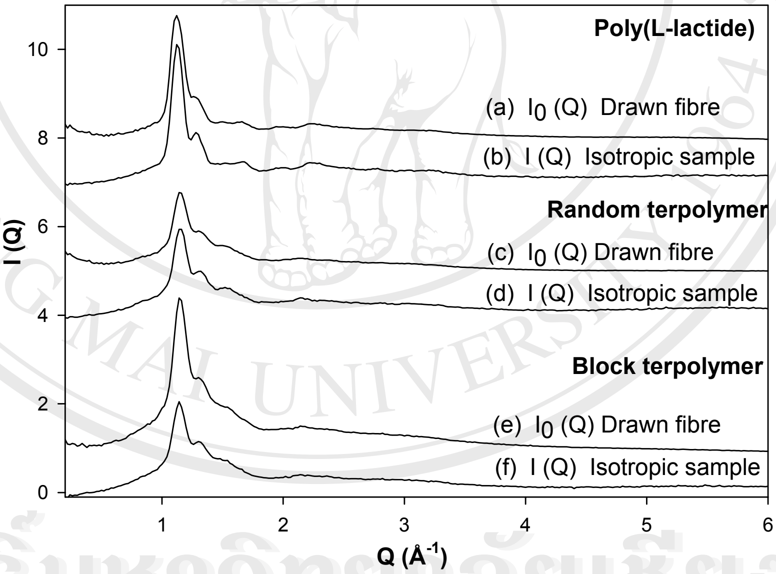

Fig. 4.33 Plots of the fully corrected and scaled wide-angle X-ray scattering intensity $\boldsymbol{I}(\boldsymbol{Q})$ recorded for samples of poly(L-lactide), random and block terpolymers crystallized from a quiescent melt (isotropic sample) compared to the azimuthally averaged data $\boldsymbol{I}_0(\boldsymbol{Q})$ for each annealed fibre as described in the text. The azimuthally averaged data represents a sample with no global preferred orientation but the same localized structure as the fibres.

In order to compare the scattering from these isotropic samples with that from the fibres, we have calculated the scattering expected for an isotropic sample with the same structure as the hot-drawn fibres. Experimentally, this could be achieved by powdering the fibre into small parts, which are then arranged randomly. However, it is more straightforward to perform the azimuthal averaging numerically using the scattering pattern for each fibre. The scattering pattern for a sample containing the same fibrous structure but with the fibre axis arranged at every angle possible with respect to the scattering vector is given by:

$$\boldsymbol{I}_{isotropic}(\boldsymbol{Q}) = \int_{0}^{\pi/2} \boldsymbol{I}(\boldsymbol{Q},\alpha)\sin\alpha d\alpha \qquad (4.20)$$

Comparison of equations 4.9 and 4.20 shows that $\boldsymbol{I}_{isotropic}(\boldsymbol{Q})$ is equivalent to $\boldsymbol{I}_0(\boldsymbol{Q})$ (as in Fig. 4.31(a)) and these functions are also plotted in Fig. 4.33. We can see that the curves are essentially the same in terms of peak positions and overall shapes. In the case of the block terpolymer, the height of the intense peak at $\boldsymbol{Q} \sim 1.2\text{Å}^{-1}$ in the curve for the isotropic sample is somewhat smaller than derived from the fibre pattern showing that that hot-drawing and annealing has increased the level of crystallinity. This effect is very much less marked in the case of the random terpolymer and in poly(L-lactide).

4.5 Discussion

Fibre diffraction studies are conventionally performed on highly aligned fibres which have often been extensively treated to enhance the levels of crystallinity; the work of Sasaki, S. et al. [88] is an example where the fibre has been treated to degrade the polymeric structure in order to enhance the crystallinity. In this work, crystallinity and alignment were enhanced by hot-drawing followed by annealing of fibres. Subsequently, a new tool in the study of fibres which allows the X-ray scattering patterns for structures with differing levels of preferred orientation to be compared directly has been introduced. The method employs a representation of the data as a series of spherical harmonics. The methodology has been applied to two terpolymers with rather different architectures but both involving sequences of randomly distributed lactide units with sequence lengths of ~ 10 (see section 2.6.5), although their positioning in the molecular chain differs. Highly -drawn monofilaments prepared have shown that both systems exhibit a semi-crystalline structure in which the lactide units crystallize in a structure equivalent to the α-phase of poly(L-lactide). Of course there are some limitations to this novel approach but the two annealed terpolymer fibres exhibit structures equivalent to the α-phase of poly(L-lactide).

A particular feature of this new approach can be used to study the crystalline structure of fibres more relevant to application, for example with the biodegradable terpolymers studied here, use as absorbable sutures is promising application. In the low draw ratio terpolymer fibres, it is clear that despite the lower level of orientation and rather small crystal size (~20-30Å) the crystal structure remains largely the same.

Comparison of the annealed and unannealed fibre patterns and associated sections shows the significant effect of annealing on the apparent crystal size (see section 4.4.1 and 4.4.2). This is more marked for the block terpolymer system. Comparison of scattering obtained from samples prepared via a quiescent melt phase shows that the drawing process does not affect the crystal structure but it does influence the level of crystallinity most markedly in the block terpolymer system. This system exhibits a maximum in the crystallization rate for quiescent systems at a slightly higher temperature than that recorded for the random terpolymer. This can be related to the differences in T_m and T_g for the two terpolymers, essentially the peak crystallization rates occur at the same level of undercooling midway between T_m and T_g. The increased level of crystallinity in the case of the block terpolymer after drawing was attributed to the enhanced mobility of the end blocks in the block terpolymer system. No evidence was seen of any microphase segregation in the block terpolymer melt prior to hot-drawing which might also influence the rate of crystallization. However, it is clear that on the larger scale the two phase crystalline/non-crystalline structure is rather ill-defined in the block terpolymer case. This is attributed to the range of block lengths present in the polymer chains and the rather disrupting (i.e. non-inclusion) effect of the highly disordered central block containing very short sequences of both lactide and caprolactone. In contrast, the random terpolymer exhibits a rather well defined two-phase structure which we attribute to the greater extent that non-lactide units can be incorporated into the interfaces of lamellar crystals to provide a smoother crystal face. This variation in the structure and dynamics of two materials with similar chemical composition but rather different architectures will be most helpful in the optimization of these materials for use in biomedical applications.